TOPICAL REVIEW

Recent developments in complex metal oxide photoelectrodes

IOP Publishing Journal of Physics D: Applied Physics

J. Phys. D: Appl. Phys. **50** (2017) 193002 (22pp) https://doi.org/10.1088/1361-6463/aa6738

Topical Review

Recent developments in complex metal oxide photoelectrodes

Fatwa F Abdi and Sean P Berglund

Helmholtz-Zentrum Berlin für Materialien und Energie GmbH, Institute for Solar Fuels, Hahn-Meitner-Platz 1, 14109 Berlin, Germany

E-mail: fatwa.abdi@helmholtz-berlin.de and sean.berglund@helmholtz-berlin.de

Received 28 December 2016, revised 3 March 2017
Accepted for publication 16 March 2017
Published 10 April 2017

Abstract

Photoelectrochemical (PEC) water splitting, a process that directly produces hydrogen from water and sunlight using semiconductor materials, is an attractive form of renewable energy production. The hydrogen that is produced can be easily transported, stored, and utilized as a fuel without the emission of greenhouse gasses. However, many scientific and engineering challenges need to be overcome before PEC water splitting can be implemented on a large scale. One of the biggest challenges is the identification of suitable semiconductor materials to use in the construction of photoelectrodes. This topical review highlights a promising class of materials, complex metal oxides, which can be used as photoelectrodes for PEC water splitting. The advantages and limitations of complex metal oxides are first discussed, and strategies to overcome the limitations are outlined using the model case of bismuth vanadate ($BiVO_4$), one of the highest performing complex metal oxide photoanodes reported to date. Building on the success story of $BiVO_4$, we discuss pathways towards achieving even higher water splitting performance, including bandgap engineering as well as the development of alternative complex metal oxides with more appropriate bandgaps for obtaining high solar-to-hydrogen efficiency. Several classes of complex metal oxides (e.g. delafossites, tungstates, vanadates, spinels) are presented as promising candidates for photoelectrode materials. Finally, we conclude by summarizing the key properties of these complex metal oxides and providing an outlook towards expedited discovery of new and novel complex metal oxides for use as photoelectrodes.

Keywords: solar water splitting, metal oxide, semiconductor photoelectrodes, complex oxides, photoelectrochemical water splitting, $BiVO_4$

(Some figures may appear in colour only in the online journal)

1. Introduction

1.1. Photoelectrochemical water splitting

In recent decades, growing concerns of finite resources as well as the environmental implications of burning fossil fuels have driven the development of various renewable energy technologies. Sunlight is by far the most abundant source of sustainable energy, but it is currently challenging to use it on a TW scale due to its intermittent nature (e.g. day-night cycle, seasonal variations). In order to solve this challenge, solar energy needs to be stored in a transportable form for an infinite amount of time. One way to achieve this is by producing chemical fuels with sunlight; chemical fuels indeed have the highest energy and power density (per mass)—up to two orders of magnitude higher than batteries or supercapacitors. Photoelectrochemical (PEC) water splitting is one of the most well studied methods to produce chemical fuels (the term 'solar fuels' is commonly used). While one can technically already split water electrochemically with a conventional photovoltaic

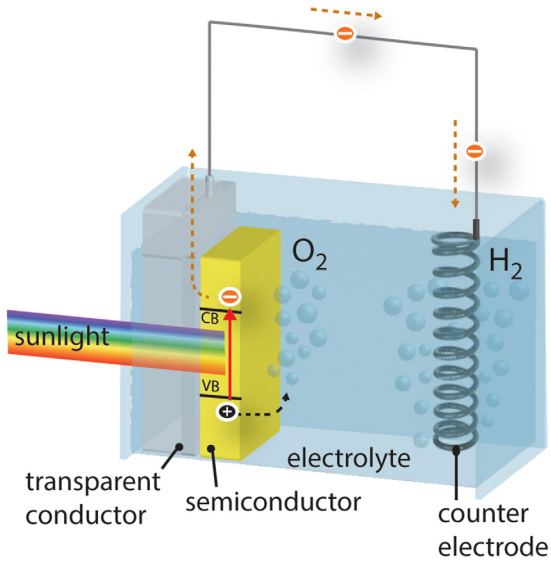

Figure 1. Schematic diagram of a PEC cell setup consisting of an n-type semiconductor and a metal counter electrode. The photo-generated holes arrive on the surface of the semiconductor and oxidize water, while the photo-generated electrons are transported to the metal counter electrode and reduce water producing hydrogen gas.

(PV)-electrolysis system, PEC water splitting integrates both light absorption and electrochemistry functionalities in the semiconductor, which may result in a cheaper and simpler approach. In short, the PEC water splitting process utilizes semiconductor photoelectrodes to absorb sunlight and generate photo-excited charge carriers (electrons and holes), which drive the water-splitting (oxidation or reduction) reactions on its surface. Figure 1 shows the schematic illustration of a PEC cell based on an n-type semiconductor and a metal counter electrode, both immersed in aqueous electrolyte. Upon illumination, the semiconductor absorbs light with an energy larger than its bandgap, and converts these photons to electron–hole pairs. In an n-type semiconductor, the photo-generated holes are swept toward the semiconductor/electrolyte interface, and the photo-generated electrons are swept toward the semiconductor/transparent conductor interface. The holes then oxidize water according to the following half-reactions:

$$\text{Alkaline electrolyte: } 4OH^- + 4h^+ \rightarrow 2H_2O + O_2$$

$$E_{ox} = +0.401 \text{ V versus NHE}$$

$$\text{Acidic electrolyte: } 2H_2O + 4h^+ \rightarrow 4H^+ + O_2$$

$$E_{ox} = +1.229 \text{ V versus NHE.}$$

At the other side of the PEC cell, the electrons are transported to the metal counter electrode (e.g. platinum), where they will reduce water and produce hydrogen according to the following half-reactions:

$$\text{Alkaline electrolyte: } 4H_2O + 4e^- \rightarrow 2H_2 + 4OH^-$$

$$E_{red} = -0.828 \text{ V versus NHE}$$

$$\text{Acidic electrolyte: } 4H^+ + 4e^- \rightarrow 2H_2$$

$$E_{red} = 0.0 \text{ V versus NHE.}$$

The water oxidation and reduction reactions are often termed the oxygen evolution reaction (OER) and hydrogen evolution reaction (HER), respectively. The same processes occur for PEC water splitting using a p-type semiconductor, except that water is reduced at the semiconductor/electrolyte interface and oxidized at the counter electrode. Based on these specific half-reactions that take place at the semiconductor surface, an n-type semiconductor photoelectrode in PEC water splitting is called a photoanode (for oxidation reactions), and a p-type semiconductor is called a photocathode (for reduction reactions).

Despite the promise of PEC water splitting, progress towards commercialization has been hindered by the lack of ideal materials that fulfil the stringent requirements. Ideal materials for PEC water splitting must meet the following criteria: (i) the semiconductor system must generate sufficient photo-voltage to split water, (ii) the bandgap of the semiconductors must ensure significant absorption of the solar spectrum, (iii) the band edge positions at the photoelectrode surfaces must straddle the redox potentials for water oxidation and reduction, (iv) the system must exhibit long-term stability under illumination in aqueous electrolytes, (v) the charge transfer from the surface of the photoelectrodes to the solution (for the OER or HER) must be facile to minimize the required kinetic overpotential and reduce energy losses, and finally (vi) the system must consist of cheap, abundant elements.

1.2. Tandem PEC water splitting system

To relax the material requirements for water splitting, tandem approaches have been taken, in which two (or more) semiconductors with varying bandgap energies are used in a system; a small-bandgap semiconductor is stacked behind a large-bandgap semiconductor. In this configuration, short-wavelength photons are absorbed in the large-bandgap semiconductor. The long-wavelength photons, which are transmitted by the large-bandgap semiconductor, are then available to be absorbed by the small-bandgap semiconductor. A variety of approaches can be used in the design of a tandem PEC device including a paired photoelectrode system (photoanode combined with photocathode) or photoelectrode combined with a photovoltaic solar cell (photoelectrode-PV). In both cases the photoelectrode must be capable of providing a relatively high photocurrent density (>8.2 mA cm^{-2}) in order to obtain high solar-to-hydrogen (STH) efficiencies (>10%). STH efficiency is linearly related to the photocurrent density (J) as follows:

$$\text{STH efficiency} = \frac{J(1.23 \text{ V})\eta_F}{P_{AM1.5}} \quad (1)$$

where the free energy change of the water splitting reaction is 1.23 eV/e$^-$, η_F is the Faradaic efficiency, and $P_{AM1.5}$ is power of solar irradiation (100 mW cm^{-2}) [1]. The theoretical maximal photocurrent density (J_{max}) of a material in mA cm^{-2} can be estimated by integrating of the AM1.5 solar spectrum above the bandgap energy (E_g) according to the following equation:

$$J_{max} = \int_{\frac{hc}{E_g}}^{280\,\text{nm}} q\Phi_{AM1.5}(\lambda)\text{d}\lambda \left(\frac{\text{mA}}{10^{-3}\,\text{A}}\right) \quad (2)$$

where, $\Phi_{AM1.5}(\lambda)$ is the solar photon flux ($cm^{-1}\ s^{-1}\ nm^{-1}$), λ is wavelength of light (nm), q is the electronic charge (1.602×10^{19} C), h is Planck's constant (4.136×10^{-15} eV s), and c is the speed of light (3×10^{17} nm s^{-1}). Note that this equation overestimates the realistically obtainable photocurrent density because it does not take into account blackbody radiation and spectrum losses but it can be used as a first pass comparison of different semiconductor materials [2, 3]. For a tandem device consisting of paired photoelectrodes the operating photocurrent density (J_{OP}) is determined by the overlap in photocurrent density of each absorber layer; the valence band of the photoanode and the conduction band of the photocathode must provide the overpotentials for the OER and HER, respectively [4, 5]. Therefore it is important that both electrodes have an early onset potential or large potential difference ($\Delta\varphi$) between the photocurrent onset (typically determined by the flat-band potential, φ_{FB}) and the electrochemical potentials for the OER or HER. The theoretical maximal potential differences are defined as follows:

$$\Delta\varphi_{max} = 1.23\ \text{V versus RHE} - \varphi_{FB}\ \text{(photoanode)} \quad (3)$$

$$\Delta\varphi_{max} = \varphi_{FB} - 0.0\ \text{V versus RHE (photocathode)}. \quad (4)$$

For a photoelectrode-PV tandem system the OER and HER overpotentials (η_{OER} and η_{HER}) must be factored in separately so that the total voltage supplied is reduced by these overpotentials; η_{HER} for a photoanode-PV system and η_{OER} for a photocathode-PV system. For state-of-the art electrocatalysts the η_{OER} and η_{HER} values can be estimated at 300 mV and 40 mV, respectively [6]. Therefore slightly higher demands are placed on the photocathode than a photoanode when used in a photoelectrode-PV system compared to a paired photoelectrode system.

1.3. (Complex) metal oxides as photoelectrodes

Among the possible materials used as photoelectrodes, metal oxides offer many unique advantages. First, metal oxides are generally stable. Since they are already oxidized they are not susceptible to oxidation when used as photoanodes. Second, metal oxides offer a variety of different bandgap energies including the medium-large range of 1.5–2.3 eV [7, 8]. This bandgap energy range is required for the top absorber in a dual absorber (tandem) PEC device in order to obtain at least 10% STH efficiency [4, 9, 10]. Lastly, metal oxides can be composed of many different elements, some of which are abundant and inexpensive to produce. This includes the alkali, alkaline, transition, and post-transition metals. So far, the majority of the efforts have been placed on simple binary metal oxides (one metal cation and oxygen anion) especially TiO_2, WO_3, and Fe_2O_3; unfortunately with limited success. Almost all possible binary metal oxide combinations have been investigated for PEC water splitting, but the ideal material remains elusive. This is where complex or multinary (ternary, quaternary, etc) metal oxides present the biggest advantage. More than 8000 and 700 000 combinations are possible with ternary and quaternary, respectively. Most of these materials have not yet been fully characterized as photoelectrodes [11], and it is likely that within these immense possibilities we may be able to find the desired photoelectrode material.

This topical review highlights the recent developments of complex metal oxides as photoelectrode materials for water splitting. This includes their general limitations and examples of successfully addressing these limitations from the model case of $BiVO_4$ as a photoanode material. It also describes alternative promising classes of complex metal oxides and addresses the future outlook of this field of research.

2. General limitations of complex metal oxides

Several limitations or challenges exist for complex metal oxides when they are used as photoelectrodes. First, as is obvious from the vast amount of possible candidates, it is definitely not trivial to screen for an ideal photoelectrode material. Combinatorial efforts have been initiated, and will be discussed in the later section of this paper. Second, the synthesis process of these complex metal oxides may also present additional challenges. This is related to the fact that there are multiple cations in a complex metal oxide, and a minor sub-stoichiometry is usually unavoidable. As an illustration, a mere 0.1% sub-stoichiometry already corresponds to a defect concentration of ~10^{19} cm^{-3}. This sub-stoichiometry is usually obtained due to lack of accurate control of metal precursor ratios during synthesis. In addition, since the synthesis process is usually done at high temperature, the different metal cations may have different vapor pressures under the heat treatment condition, resulting in selective loss of one of the elements. Such a large amount of defects may have a very undesirable effect on the performance of the photoelectrode, i.e. the defects may act as recombination centers and kill the photoactivity. Finally, most metal oxides have relatively poor carrier transport properties. This is definitely true as compared to many common covalent semiconductors, such as Si and III–V (e.g. GaAs) materials. The poor properties of complex metal oxides have been related to the nature of carrier localization; carriers generally are transported via a polaron hopping mechanism, which results in relatively low carrier mobility [12].

3. The success story of $BiVO_4$

Despite the limitations mentioned above, there are several examples in the literature where high photocurrents have been achieved with complex metal oxides. One particular success story is the development of bismuth vanadate ($BiVO_4$) as a photoanode. $BiVO_4$ has attracted a significant amount of interest in the past few years. This is reflected in the exponential increase in the number of publications on $BiVO_4$ in the field of photo(-electro)chemistry, as shown in figure 2. In 2015 alone, there were ~300 publications on $BiVO_4$. These concerted efforts have resulted in $BiVO_4$ being the current highest performing metal oxide photoanode.

$BiVO_4$ has three polymorphs: pucherite, dreyerite and clinobisvanate. The most photoactive phase is clinobisvanate, which has a monoclinic (scheelite-type) crystal structure

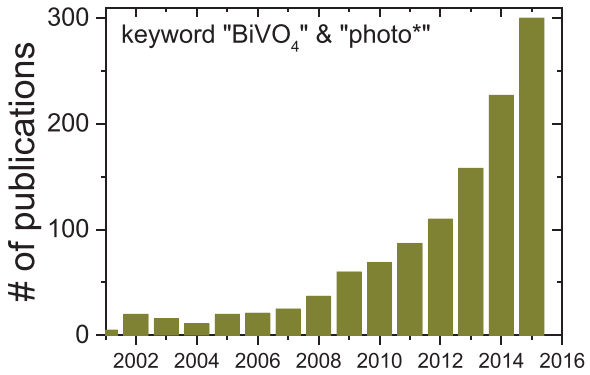

Figure 2. The number of publications recorded in the Web of Science database using keywords '*$BiVO_4$*' and '*photo**'. The exponential increase in recent years represents the growing interest on $BiVO_4$ as a photocatalytic and photoelectrode material.

(space group *C*2/*c*, $a = 7.247$ Å, $b = 11.697$ Å, $c = 5.09$ Å, and $\beta = 134.226°$) [13, 14]. Figures 3(a) and (b) show the crystal structure of clinobisvanate $BiVO_4$, which consists of VO_4 tetrahedra and BiO_8 dodecahedra. Each O atom is coordinated to one V center and two Bi centers. The local environments of Bi and V are however distorted, resulting in the loss of the fourfold symmetry [13]. This distortion has been claimed to be responsible for the higher photocatalytic activity, as compared to the other polymorphs [15, 16]. A processing temperature of higher than 400 °C is normally required to obtain the monoclinic clinobisvanate phase [16–18].

The monoclinic phase has been reported to have a bandgap of ~2.4–2.5 eV [16, 19, 20]. The electronic structure of $BiVO_4$ has been thoroughly investigated by many researchers, both theoretical and experimental [14, 19–26]. However, the nature of the optical transition in the monoclinic scheelite $BiVO_4$ (i.e. the composition of the valence band and the directness of the transition) had been the subject of controversy in the literature. Initially, it was proposed that the optical transition occurs from Bi 6*s* or hybrid Bi 6*s*–O 2*p* orbitals and empty V 3*d* orbitals [16]. This was later proven to be unlikely. The crystal distortion in monoclinic $BiVO_4$ pushes the O 2*p* states upward and reduces the bandgap, but the optical transition still occurs between the filled O $2p_\pi$ and empty V 3*d* orbitals [21, 26]. Cooper *et al* performed a thorough combination of advanced spectroscopic analysis and DFT calculations to reveal the electronic structure [19, 20], as shown in figure 3(c). They revealed that the optical transition is indirect in nature, with the direct transition occurring at slightly higher energies (~200 meV).

$BiVO_4$ has been investigated as a photocatalyst and photoelectrode material since late 1990s/early 2000s [15, 16, 27–30]. These early efforts, however, only resulted in modest photocurrent densities (several hundreds of μA cm^{-2}). A few years ago, researchers started to focus on identifying the factors that limited the performance of $BiVO_4$. The first identified limitation was slow transfer of photo-generated holes from the surface of the $BiVO_4$ to the electrolyte. This was shown by many studies that utilized hole scavengers, such as hydrogen peroxide, methanol, and sulfites [28, 31–37]. To solve this, surface modification layers have been applied on $BiVO_4$. For example, in our lab, we electrodeposited a ~30 nm cobalt phosphate (Co–Pi) catalyst layer on our spray pyrolysed $BiVO_4$ [31, 32]. As shown in the AM1.5 photocurrent–voltage curve of figure 4, the photocurrent is significantly increased from the bare $BiVO_4$ (black curve) to the Co–Pi catalyzed $BiVO_4$ (red curve). The Co–Pi was initially assumed to increase the catalytic activity of the surface of $BiVO_4$, but recent studies have indicated that the more likely cause is that Co–Pi decreases the surface recombination on $BiVO_4$ [38–40]. Either way, the charge transfer efficiency of the photogenerated holes increases after this surface modification. Other oxygen evolution catalysts (OEC) have also been investigated and many of them (e.g. cobalt and nickel borate, iron oxyhydroxide, nickel oxyhydroxide) [35, 36, 41–43] are also effective in overcoming this limitation of $BiVO_4$.

After the charge transfer limitation was addressed, the poor carrier transport properties of $BiVO_4$ started to limit the performance. As in many metal oxides, charge carriers are transported via a small polaron hopping conduction mechanism [44]. Both electron and hole polarons exist in $BiVO_4$; they are predicted to be located at ~0.3 eV below the conduction band and ~0.9 eV above the valence band, respectively [45, 46]. We recently showed for the first time direct evidence of hole polarons in $BiVO_4$ using THz spectroscopy [47]. The THz photoconductivity spectra for $BiVO_4$ is shown in figure 5(a). In short, we observed two distinct regimes: Drude–Smith behavior explains the spectrum lower than 1.7 THz, and a damped harmonic oscillator model explains the spectrum above 1.7 THz. The latter is associated to strong carrier localization, and we have shown that this can be assigned to be the signal of hole polarons [47]. Electron polarons in $BiVO_4$ have also been indirectly observed via temperature-dependent conductivity measurements, electron paramagnetic resonance spectroscopy, and x-ray absorption spectroscopy [39, 44, 48, 49]. Overall, this polaron conduction mechanism results in relatively low charge carrier mobility in $BiVO_4$. A value of 0.02 cm^2 V^{-1} s^{-1} was reported for a polycrystalline $BiVO_4$ [50], and only one order of magnitude higher for a single crystal $BiVO_4$ [44]. These values are few orders of magnitude lower as compared to Si (1500 cm^2 V^{-1} s^{-1} for electron and 450 cm^2 V^{-1} s^{-1} for hole) [51] or even other commonly studied oxides, e.g. ZnO (200 cm^2 V^{-1} s^{-1} for electron and 180 cm^2 V^{-1} s^{-1} for hole) [51, 52].

To compensate the low charge carrier mobility, doping has been applied to increase the carrier concentration in $BiVO_4$, and hence the conductivity. Tungsten (W) and molybdenum (Mo) are the two most effective dopants used in $BiVO_4$ [31, 53–55]. They both have 6 valence electrons; substitution of V^{5+} with W^{6+} or Mo^{6+} results in donor-doped $BiVO_4$. While it has been shown to be effective to a certain degree, doping also has a negative influence on the carrier transport properties of $BiVO_4$. Increasing dopant concentration will result in decreasing the width of the space charge layer, and thus decreasing the efficiency of charge separation. One way to overcome this trade-off is to create a distributed n^+-n homojunction [56]. The concept was first applied in our lab and is illustrated in figure 5(b). For a homogeneously-doped W-$BiVO_4$, space charge layer is only present at the surface of

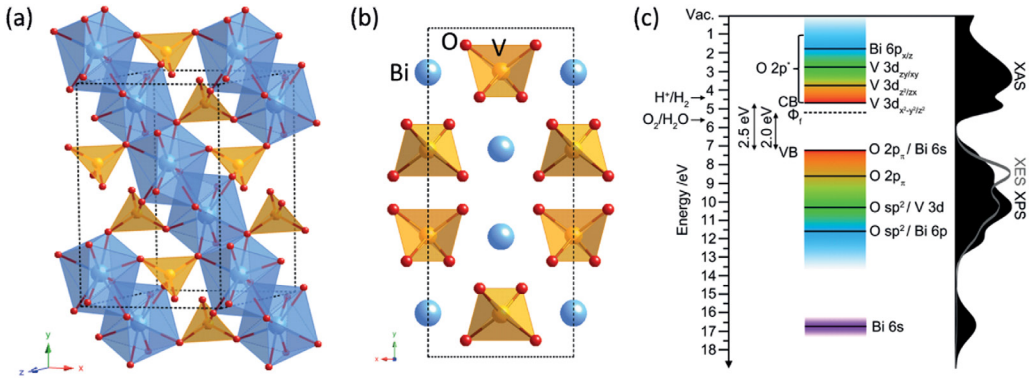

Figure 3. (a) Crystal structure of the clinobisvanite (monoclinic scheelite) polymorph of $BiVO_4$. (b) The side view (*c*-axis) of the structure. (c) Electronic structure of the clinobisvanite $BiVO_4$, as revealed by DFT calculation as well as XAS, XES and XPS measurements. Reprinted with permission from Cooper *et al* [19]. Copyright 2014 American Chemical Society.

the $BiVO_4$. Photogenerated carriers in the bulk of the $BiVO_4$ are therefore not driven by an internal electric field, only by diffusion. However, by taking advantage of the Fermi level difference between $BiVO_4$ with a varying dopant concentration, we designed a $BiVO_4$ film with a 10-step W dopant gradient and distributed the internal electric field throughout the bulk of the $BiVO_4$. As a result, the carrier separation efficiency increased from ~38% to more than 60% at 1.23 V versus RHE [56]. The overall AM1.5 photocurrent of the $BiVO_4$ photoanode was therefore increased significantly by applying this simple gradient dopant concept, as shown in figure 4 (blue). The gradient dopant concept is a generally applicable strategy to increase the charge separation efficiency in highly doped semiconductors; several other studies on other semiconducting photoelectrodes have also reported the effectiveness of the concept [57–59].

The next limitation of $BiVO_4$ is the modest optical absorption. This is especially true for the wavelengths close to the bandgap of $BiVO_4$. One way to overcome this limitation is to introduce metallic nanoparticles (e.g. Ag, Au, $Ag@SiO_2$) [60–62] and take advantage of the plasmonic resonance effect. Another method is to simply replace the back substrate of the photoelectrode (typically FTO-coated glass) with a textured substrate [56, 63]. This relatively straightforward method was used to our Co–Pi catalyzed, gradient-doped W–$BiVO_4$, and the AM1.5 photocurrent was again improved to >4 mA cm^{-2} (see figure 4).

Nanostructuring has also been shown to be an effective strategy to overcome the limitations of $BiVO_4$. Both the carrier transport and optical absorption limitations can be essentially tackled by nanostructuring. The charge carrier diffusion length in $BiVO_4$ has been reported to be ~70–100 nm [44, 50]. In a nanostructured $BiVO_4$ with feature sizes smaller than this diffusion length, most of the charge carriers can be collected at the surface or interface before they recombine, and high carrier separation efficiency can be obtained. Electrodeposited porous $BiVO_4$ with a particle size in the range of ~70–80 nm indeed showed carrier separation efficiencies of higher than 90% at 1.23 V versus RHE [35]. Guest-host nanostructure concept has also been explored by depositing a thin conformal layer of $BiVO_4$ on top of WO_3 nanowires or nanoporous films [37, 64–67]. For example, Pihosh *et al* fabricated WO_3

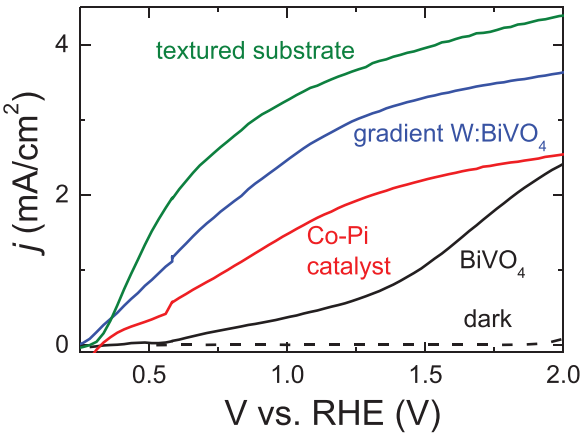

Figure 4. AM1.5 photocurrent–voltage curve of bare $BiVO_4$ (black), Co–Pi catalyzed $BiVO_4$ (red), Co–Pi catalyzed gradient W-doped $BiVO_4$ (blue), and Co–Pi catalyzed gradient W-doped $BiVO_4$ deposited on a textured FTO substrate (green). The electrolyte in all cases was 0.1 M potassium phosphate buffer (pH ~ 7) and the scan rate was 50 mV s^{-1}.

nanorods via glancing angle deposition (GLAD) and electrodeposited CoPi catalyzed thin $BiVO_4$ layer (~50 nm) on top of the nanorods (see figure 6) [66]. With this electrode, they reported an AM1.5 photocurrent of 6.7 mA cm^{-2} at 1.23 V versus RHE. At the time of the writing, this is the highest AM1.5 photocurrent ever reported for $BiVO_4$.

Stability is an important criteria for photoelectrodes. Early reports have suggested that $BiVO_4$ is stable within the pH range of 3–11 [68]. However, more detailed examinations of the stability and construction of the Pourbaix diagram revealed that polycrystalline $BiVO_4$ thin films are susceptible to chemical and photochemical corrosion, even in the neutral pH range [69]. Surface modification of $BiVO_4$ with co-catalysts and/or protection layers were usually applied in order to improve the stability of $BiVO_4$ photoelectrodes. As a result, long-term stable photocurrents in neutral pH (>1000 h) and pH 13 solution (several hours) have been recently demonstrated [70–72].

The progress of $BiVO_4$ photoanodes is summarized in figure 7, where the AM1.5 photocurrents at 1.23 V versus RHE of various reported $BiVO_4$ photoanodes are plotted. Prior to 2010, only very small improvements were reported. Beyond 2010, the photocurrent increased much more rapidly, which

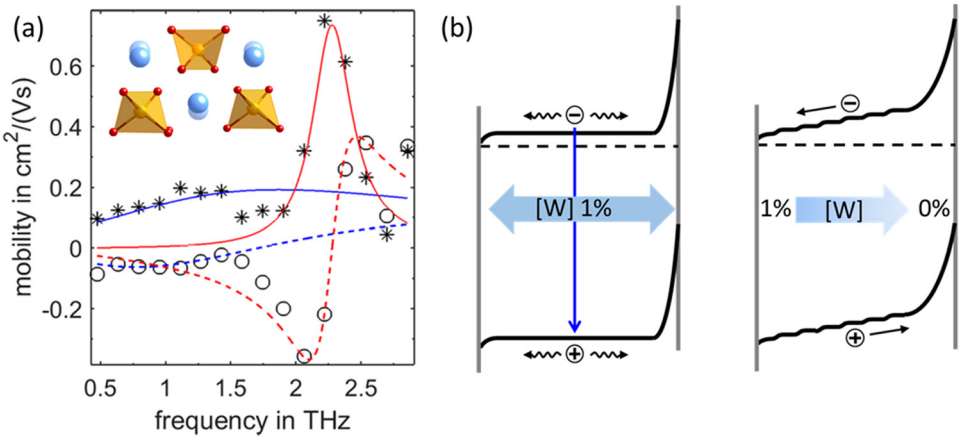

Figure 5. (a) THz combined electron−hole mobility spectrum of a $BiVO_4$ film at 10 ps delay time fitted with the Drude–Smith model at lower frequencies (real part, blue solid curve; imaginary part, blue dashed curve) and the damped oscillator model at higher frequencies (real part, red solid curve; imaginary part, red dashed curve). The real and imaginary parts of the measured conductivity are indicated by stars (∗) and open circles (○), respectively. The resonance frequency at ~2.1 THz was assigned to be the hole vibration along the Bi^{3+} and VO_4^{3-} units in the [0 1 2] direction, as shown in the inset. Adapted with permission from Ziwritsch *et al* [47]. Copyright 2016 American Chemical Society. (b) Energy band diagram of $BiVO_4$ with homogeneous W-doping (left) and gradient W-doping (right).

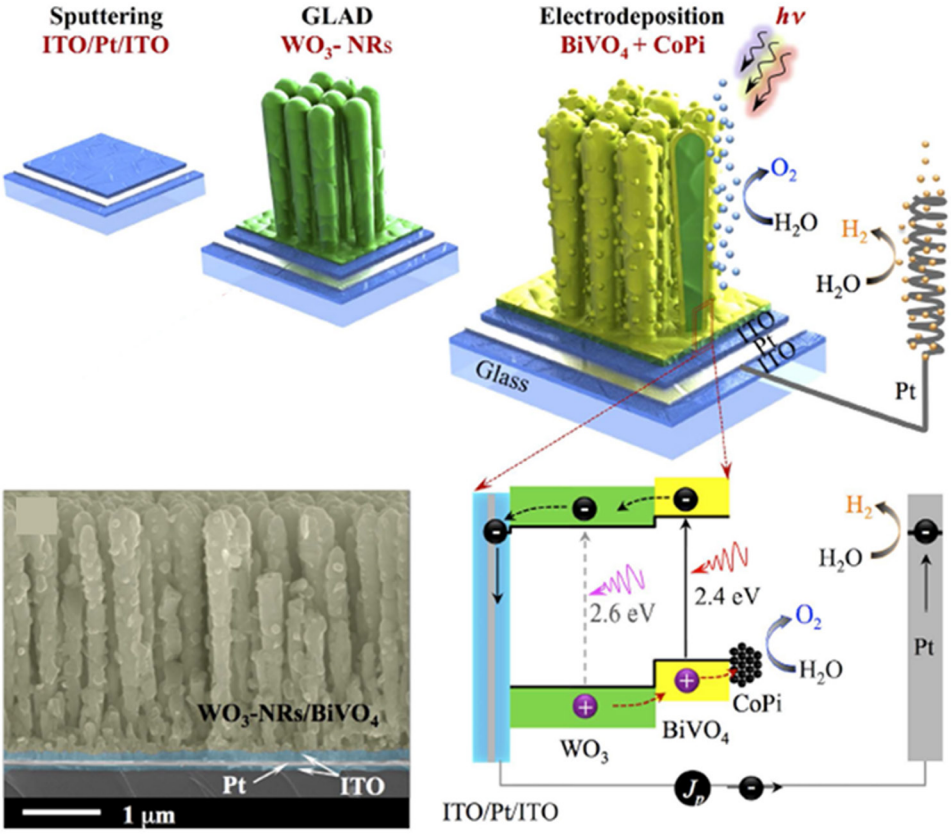

Figure 6. Schematic illustration of a core–shell WO_3-nanorods/$BiVO_4$ photoanode. The cross-section SEM image of the structure is also shown. GLAD: glancing angle deposition. Reprinted from Pihosh *et al* [66]. CC BY 4.0.

is a result of systematic investigation of the performance limiting factors and implementation of appropriate strategies as already outlined above. It is noted that this trend is very similar to the trend in the number of publications on $BiVO_4$ (figure 2). It is clear that the collective efforts of the field in the development of $BiVO_4$ has successfully resulted in establishing $BiVO_4$ as one of the highest performing metal oxide photoelectrode materials.

Figure 7 also shows the theoretical maximum photocurrent (J_{max}) that can be obtained by a $BiVO_4$ photoelectrode. This is shown as the horizontal blue line at the photocurrent level of ~7.5 mA cm^{-2}. This value assumes that all photons in the AM1.5 spectrum with energies larger than the bandgap of $BiVO_4$ (2.4 eV is taken here) can be absorbed and collected as photocurrents with 100% efficiency. From this plot, it is obvious that the difference between this theoretical limit and the

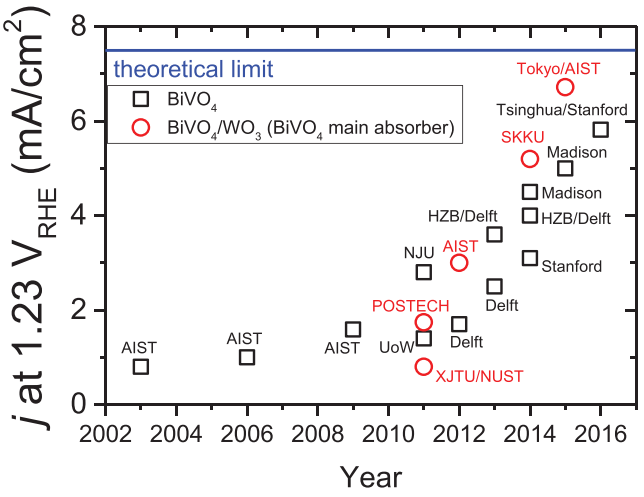

Figure 7. Reported photocurrent of $BiVO_4$ (black squares) and $BiVO_4/WO_3$ guest-host (red circles) photoanodes at 1.23 V versus RHE. Except for the first two points from AIST, the photocurrents were measured under AM1.5 illumination. Data were extracted from various reports in the literature [28, 31–33, 35–37, 56, 63–66, 73–79]. The theoretical maximum photocurrent for $BiVO_4$ based on its bandgap of 2.4 eV is shown as the horizontal blue line.

highest reported photocurrent is already very close. The 6.7 mA cm^{-2} photocurrent reported by Pihosh *et al* [66] is within 10% of the theoretical maximum. This achievement of $BiVO_4$ illustrates that despite the many challenges that may be posed by complex metal oxides (e.g. polaron conduction mechanism, high defect concentration), a highly efficient photoelectrode can still be obtained by implementing appropriate strategies. In other words, these limitations should not be used to justify the exclusion of complex metal oxides (or metal oxides in general) as candidate materials for photoelectrochemical water splitting.

Several unassisted solar water splitting devices have also been fabricated based on $BiVO_4$ photoelectrodes. In all cases, the $BiVO_4$ photoelectrodes were combined in a tandem configuration with a second absorber (usually a solar cell). The blue part of the solar spectrum is absorbed by the $BiVO_4$ and the red part, which is transmitted by $BiVO_4$, is absorbed by the solar cell behind the $BiVO_4$ photoelectrode and used to provide the necessary bias potential. The first $BiVO_4$-based tandem device was reported by our lab [56], as shown in figure 8(a). Here, a Co–Pi catalyzed gradient-doped W–$BiVO_4$ was combined with a thin film amorphous silicon solar cell [56, 63]. STH efficiencies of 3.6, 4.9 and 5.2% were obtained with single-junction amorphous, double-junction amorphous, and micromorph (microcrystalline/amorphous tandem) solar cells, respectively. The highest performing $BiVO_4$ photoanode by Pihosh *et al* discussed above was also combined into an unassisted solar water splitting device with a multi-junction III–V solar cell (double-junction GaAs/InGaAsP) [66, 80]. In this case, due to the use of reflective substrate (ITO/Pt/ITO), the $BiVO_4$ photoanode was positioned in 45° with respect to the solar cell (figure 8(b)); the red part of the solar spectrum is reflected towards the solar cell. The high performance of the $BiVO_4$ as well as the III–V based solar cell resulted in an impressive STH efficiency of 8.1% [66, 80]. More recent efforts have also been focused on novel tandem concepts, such as dual photoelectrode with extended light harvesting by combining $BiVO_4$ and Fe_2O_3 photoelectrodes with *c*-Si solar cells (figure 8(c)) [81], and the inclusion of distributed Bragg reflector (DBR) in between a $BiVO_4$ photoelectrode and a dye-sensitized solar cell (figure 8(d)) [82]. STH efficiencies of 7.7% and 7.1% were reported for these novel concepts, respectively. A complete overview of all solar water splitting devices reported based on $BiVO_4$ photoelectrode is listed in table 1.

4. Beyond $BiVO_4$

To further improve the achieved STH efficiency with complex metal oxide photoelectrodes, several issues still need to be addressed. First, although the achieved AM1.5 photocurrent with $BiVO_4$ is already very close to the theoretical maximum, this is achieved at relatively high applied potential (>1.0 V versus RHE). This immediately places certain restrictions on the type of solar cells that can be used in the tandem solar water splitting device. A relatively large open circuit voltage is needed to place $BiVO_4$ at a high electrochemical potential; multi-junction solar cells are typically needed, which increases the complexity (and possibly cost) of the overall device. Efforts should therefore be placed on improving the performance of $BiVO_4$ at much lower applied potentials, i.e. increasing the fill factor (FF) of the photocurrent–voltage curve. As illustrated in figure 9, a $BiVO_4$ with a higher FF would allow the application of a simple single-junction solar cell as the tandem combination with potentially much higher STH efficiency. Recombination pathways occurring at these low potentials, either at the bulk, surface or interface of the $BiVO_4$ would need to be first identified to accomplish this.

Unfortunately, even if the FF of $BiVO_4$ could be improved to nearly ideal, only a marginal improvement in the STH efficiencies can be obtained. This is simply because $BiVO_4$ is intrinsically limited by its bandgap of 2.4 eV, which means that a maximum STH efficiency of ~9% can only be achieved. Recently, several groups of researchers have determined the optimal combination of bandgaps in a dual-absorber tandem configuration [87–90]. To achieve STH efficiencies higher than 20%, a bottom absorber with a bandgap of ~1.0–1.3 eV needs to be combined with a top absorber with a bandgap of ~1.7–1.9 eV (see figure 10). Several good options are available for the bottom absorber, such as Si and WSe_2 [91–94]. However, the choice for the top absorber is not so obvious; we therefore need to find an efficient and stable complex metal oxide within this bandgap range.

4.1. Decreasing the bandgap of complex metal oxides

One way to obtain a complex metal oxide with the desired bandgap is to modify the bandgap of a known complex metal oxide by anion substitution. Most metal oxides have rather large bandgaps since the valence band maximums are composed of mainly O 2*p* orbitals, which lay relatively low in the energy scale. Anion substitution with elements that have higher energy orbitals could potentially push the valence band upward and decrease the bandgap. An example is to partially replace oxygen ions by nitrogen ions to form oxynitrides, as illustrated in figure 11 in the case of tantalum oxynitride.

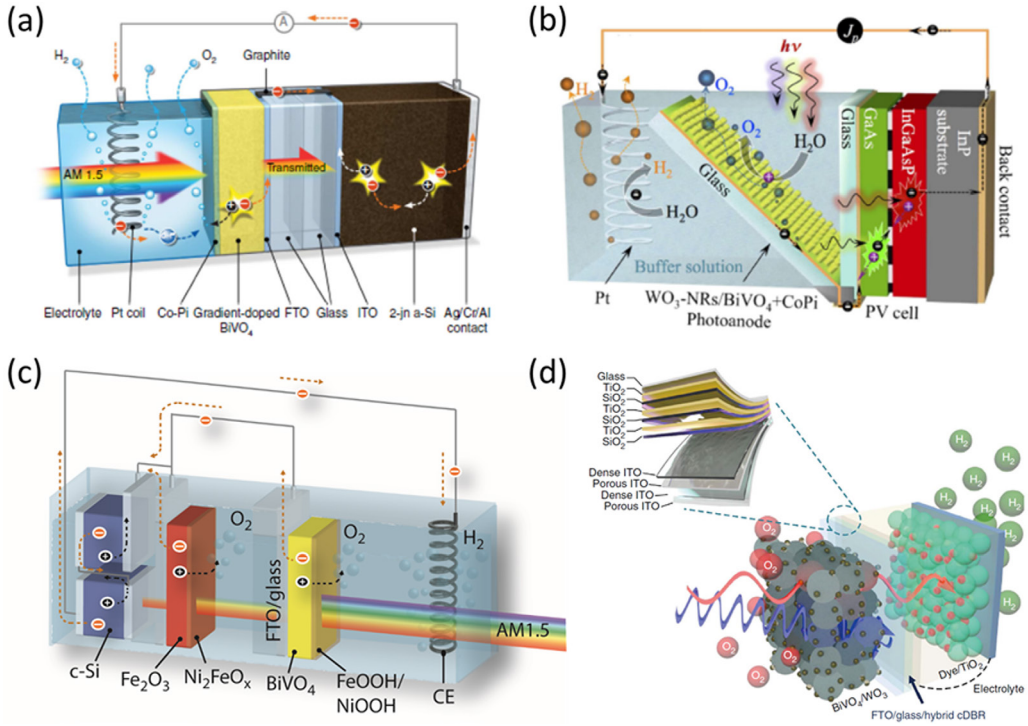

Figure 8. Various schematic structures of solar water splitting devices based on (a) $BiVO_4$ photoanode and thin film amorphous silicon solar cell (reprinted from Abdi *et al* [56]. Copyright 2013, Rights Managed by Nature Publishing Group), (b) $BiVO_4/WO_3$ nanorods photoanode and GaAs/InGaAsP solar cell (reprinted from Pihosh *et al* [66]. CC BY 4.0.), (c) $BiVO_4$–Fe_2O_3 dual photoanode and crystalline silicon solar cell (reprinted from Kim *et al* [81]. CC BY 4.0.), and (d) mesoporous $BiVO_4/WO_3$ photoanode, dye-sensitized solar cell (DSSC) and distributed Bragg reflector (DBR) (reprinted from Shi *et al* [82]. CC BY 4.0.).

Tantalum oxide (Ta_2O_5) is a stable large bandgap semiconductor ($E_g = 3.9$ eV), whereas tantalum nitride (Ta_3N_5) is a visible light absorber ($E_g = 2.1$ eV) yet unstable in aqueous solutions. To compromise between the stability and the light absorption, researchers have partially substituted the oxygen ions in Ta_2O_5 with nitrogen ions, resulting in the β-TaON with a more favorable bandgap of 2.4 eV and acceptable stability [95–99]. Photocurrents above 3 mA cm^{-2} have been shown for TaON photoanodes [95, 98].

Although the valence band maximum of $BiVO_4$ is slightly pushed upward due to the hybridization with the Bi 6*s* orbital, it is still composed of mainly O 2*p* orbitals. Partial nitrogen substitution of oxygen could therefore potentially raise the valence band and result in a bandgap lower than 2.4 eV. A first principle calculation has predicted an upward valence band shift of ~200 meV for a $BiVO_{3.9375}N_{0.0625}$ stoichiometry [100]. It is, however, not known whether this stoichiometry or any other bismuth vanadium oxynitride phases are thermodynamically possible to be formed. Kim *et al* recently reported the incorporation of nitrogen into their porous electrodeposited $BiVO_4$ [76]. They obtained the formation of $BiVO_{3.54}N_{0.31}$ with an observed absorption red shift of ~200 meV. The absorptance spectra and the photographs of the films are shown in figure 12(a). Interestingly, they performed the nitrogen incorporation by a very mild N_2 annealing treatment at 350 °C. It was suggested that this is a specific attribute of nitrogen incorporation in $BiVO_4$, but it is surprising that the relatively strong triple bond of nitrogen ($N \equiv N$) can be broken at this temperature. It should be noted that the Haber–Bosch process of producing ammonia from nitrogen and hydrogen, even in the presence of a catalyst, requires a temperature of at least 400 °C [101, 102]. The mechanism of nitrogen incorporation in $BiVO_4$ by this mild N_2 annealing therefore needs to be further elucidated.

Another way of incorporating nitrogen into metal oxides is through ion implantation. N-ion implantation has been reported for TiO_2 and ZnO photoelectrodes, and shifts of the bandgap and higher photocurrents under visible light illumination have been observed [103, 104]. A preliminary study in our lab has suggested that this may also be effective for $BiVO_4$. Through a combination of suitable ion implantation energy and post-annealing conditions, we observed an extended absorption tail up to ~750 nm, and the absorbed photons are increased by ~40%. Alternative to nitrogen, sulfur can also be incorporated into metal oxides to shift the valence band up and decrease the bandgap. This is because S 3*p* orbitals also have higher energy as compared to O 2*p* orbitals. Our preliminary results show that both the indirect and direct bandgaps are successfully reduced with increasing partial pressure of sulfur. Further analysis and studies on these nitrogen- and sulfur-incorporated $BiVO_4$ films are currently ongoing.

4.2. Novel complex metal oxides as photoelectrodes

Instead of modifying the bandgap of a known large-bandgap metal oxide (such as the case of $BiVO_4$ above), alternative complex metal oxides with small bandgap may be explored. This section highlights several classes of complex metal oxides that fulfil this requirement as either photoanodes or photocathodes.

Table 1. Reported solar water splitting devices based on $BiVO_4$ photoanodes.

$BiVO_4$ photoanode	Tandem combination	Electrolyte	STH efficiency	Stability data shown	Ref
CoPi catalyzed, gradient W-doped $BiVO_4$	a-Si solar cell	0.1 M potassium phosphate buffer (pH 7)	3.6%	1 h	[56]
CoPi catalyzed, gradient W-doped $BiVO_4$	2-jn a-Si/a-Si solar cell	0.1 M potassium phosphate buffer (pH 7)	4.9%	1 h	[56]
CoPi catalyzed, gradient W-doped $BiVO_4$	2-jn a-Si/μ-Si solar cell	0.1 M potassium phosphate buffer (pH 7)	5.2%	1 h	[63]
CoPi catalyzed gradient W-doped $BiVO_4$	RuO_x/TiO_2/Al:ZnO/Cu_2O photocathode	0.1 M potassium phosphate buffer (pH 7)	0.5%	20% loss in 2 min	[5]
CoPi catalyzed $BiVO_4/WO_3$ guest-host nanorods	2-jn GaAs/InGaAsP solar cell	0.1 M potassium phosphate buffer (pH 7)	8.1%	1 h	[66]
FeOOH/NiOOH catalyzed (W,Mo)-doped $BiVO_4/WO_3$ guest-host nanoporous	Cobalt-electrolyte DSSC and hybrid DBR stack	0.1 M sodium phosphate (pH 6.9)	7.1%	10 h	[82]
Co–Ci catalyzed H-treated Mo-doped $BiVO_4$	$CH_3NH_3PbI_3$ perovskite solar cell	0.1 M bicarbonate electrolyte (pH 7)	4.3% (wired) 3% (wireless)	12 h	[83]
Co–Pi catalyzed $BiVO_4$	$CH_3NH_3PbI_3$ perovskite solar cell	0.1 M phosphate buffer	2.5%	10% loss in 5 min	[84]
NiOOH/FeOOH catalyzed Mo-doped BiVO4	Pt/CdS/$CuGa_3Se_5$/(Ag,Cu)$GaSe_2$ photocathode	0.1 M phosphate buffer (pH 7)	0.67%	2 h	[85]
FeOOH/NiOOH catalyzed (W,Mo)-doped $BiVO_4/WO_3$ guest-host nanoporous	Cobalt-electrolyte DSSC	0.1 M sodium phosphate (pH 6.9)	5.7%	2 h	[86]
FeOOH/NiOOH catalyzed Mo-doped nanocone $BiVO_4$	Perovskite solar cell	0.5 M potassium phosphate buffer (pH 7)	6.2%	~4% loss in 10 h	[77]
FeOOH/NiOOH catalyzed H-treated Mo-doped $BiVO_4$	$NiFeO_x$ catalyzed Ti-doped Fe_2O_3 and crystalline Si solar cell	1 M potassium carbonate (pH 9.2)	7.7%	~10% in 8 h	[81]

4.2.1. Cu(I)-based oxides.

4.2.1.1. Cu_2O. Cuprous oxide, Cu_2O, is the most commonly studied Cu(I)-based metal oxide material for PEC applications. It is a p-type semiconductor with a cubic crystal structure (space group $Pn\bar{3}m$, a = 4.2696 Å) and bandgap energy of 1.9–2.2 eV resulting in a J_{max} of about −14 mA cm^{-2} [105–107]. The flat-band potential of Cu_2O is located at approximately 0.75 V versus RHE [108]. For a metal oxide, Cu_2O has an exceptionally high mobility in the range of 60–130 $cm^2\ V^{-1}\ s^{-1}$ (at ~300 K) depending on the synthesis conditions [109–111]. Cu_2O thin films have been synthesized for PV and PEC applications using a wide range of deposition techniques including electrodeposition, sol-gel, spray, and sputtering [106, 107]. However, since its first demonstration as a photocathode material, Cu_2O has been a challenging PEC material to work with because the electrochemical potential to reduce Cu_2O to Cu is more positive than the potential for water reduction, which makes Cu_2O highly susceptible to photocorrosion when illuminated in aqueous solutions [112–114]. A major breakthrough occurred in 2011, when the Grätzel group at EPFL showed that Cu_2O photocathodes could be significantly stabilized with protective coatings of Al-doped ZnO (AZO) and TiO_2 deposited by atomic layer deposition (ALD) [115]. Since then, researchers have systematically addressed the stability and photoconversion efficiency challenges of Cu_2O using various nanostructures, buffer layers, protection layers, and electrocatalysts including earth abundant NiOx, MoS_{2-x}, and Ni–Mo [116–119]. Most recently the Grätzel group achieved photocurrent densities as high as −10 mA cm^{-2} at 0 V versus RHE for Cu_2O nanowire photocathodes with AZO/TiO_2 protection layers and RuO_x catalyst loading [120]. The photocurrent density was maintained for over 55 h. Although Cu_2O is not a complex metal oxide, the most recent PEC results for Cu_2O photocathodes represent significant progress in PEC water splitting and may be useful in efforts to improve and stabilize other Cu(I)-based complex metal oxides.

4.2.1.2. Cu(I) vanadates, niobates, and tantalates. Many Cu(I) vanadates, niobates, and tantalates are p-type metal oxide semiconductors and show activity for photo-reduction reactions. The group of Maggard has studied a significant portion of these materials and summarized them in a recent review article [121]. The list of studied materials includes Cu_3VO_4 ($E_g \approx 1.20$ eV) [122], $CuNb_2O_6$ ($E_g \approx 1.9$ eV) [123], $CuNb_3O_8$ ($E_g \approx 1.26$ eV) [124, 125], $Cu_2Nb_8O_{21}$ ($E_g \approx 1.43$ eV) [126], $CuNbO_3$ ($E_g \approx 2.00$ eV) [127, 128], α-$Cu_2Ta_4O_{11}$ and β-$Cu_2Ta_4O_{11}$ ($E_g \approx 2.65$ eV) [129], $Cu_3Ta_7O_{19}$ ($E_g \approx 2.60$ eV) [130, 131], and $Cu_5Ta_{11}O_{30}$ ($E_g \approx 2.55$ eV) [130–132]. Two advantages of using these Cu(I) mixed metal oxides are that they (i) come in various bandgap energies in the visible-light range (~1.20–2.65 eV) and (ii) often show better stability under illumination in aqueous solutions compared to Cu_2O. This has been attributed to the addition of V^{5+}, Nb^{5+}, or Ta^{5+} metal cations with unfilled d orbitals allowing electrons to be excited into the conduction band of the material

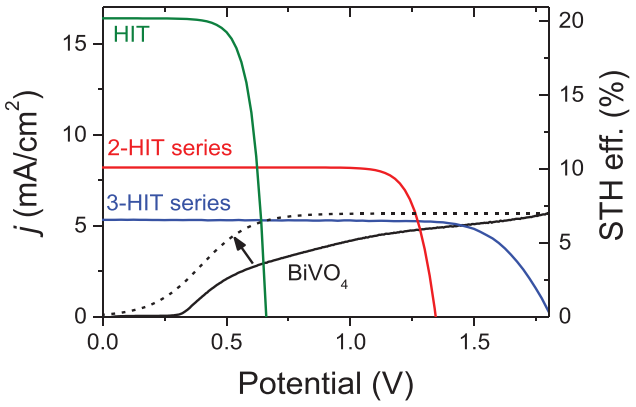

Figure 9. Photocurrent–voltage curve (left *y*-axis) of $BiVO_4$ photoanode and heterojunction (HIT) solar cells in a single, 2-series, and 3-series configurations. The black dashed line illustrates the photocurrent–voltage curve of a hypothetical $BiVO_4$ photoanode with an improved fill factor (FF). The right *y*-axis shows the respective solar-to-hydrogen (STH) efficiencies (linearly related to photocurrent according to equation (1) for the multiple $BiVO_4$-solar cell combinations, as indicated by the intersection between their photocurrent–voltage curves.

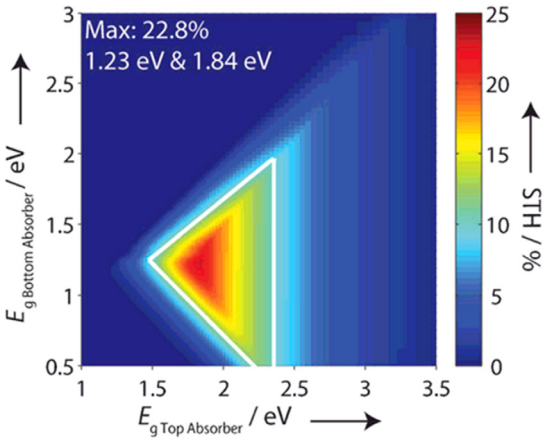

Figure 10. Solar-to-hydrogen (STH) efficiency colorplot of a dual stacked absorber configuration as a function of the bandgap of the top and bottom absorber. The white and black triangle indicates the 10% and 20% STH efficiency boundary, respectively. Adapted with permission from Seitz *et al* [87] John Wiley & Sons. © 2014 WILEY-VCH Verlag GmbH & Co. KGaA, Weinheim.

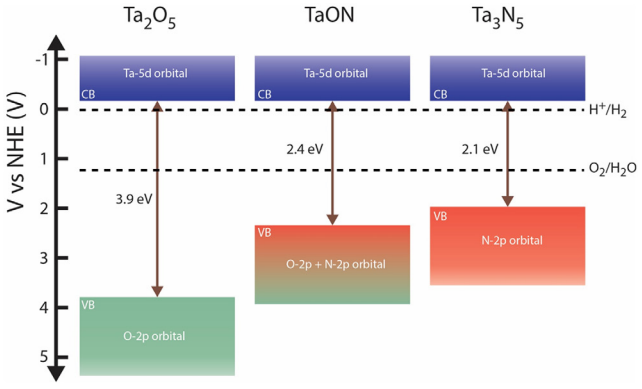

Figure 11. Band diagram of tantalum oxide (Ta_2O_5), oxynitride (TaON) and nitride (Ta_3N_5).

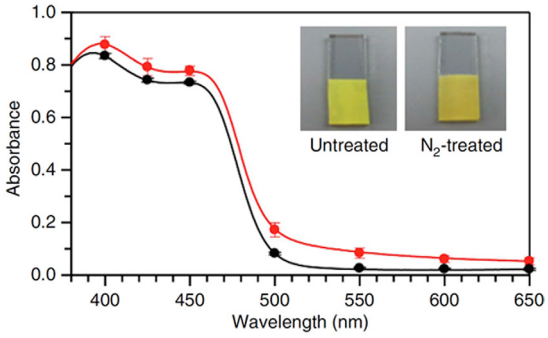

Figure 12. (a) Absorbance spectra of nanoporous $BiVO_4$ electrode (black) and N_2-annealed $BiVO_4$ electrodes (red). The photographs of both electrodes are shown in the inset. Reprinted from Kim *et al* [76]. CC BY 4.0.

(instead of the Cu^+ *d* orbitals that form the conduction band of Cu_2O), inhibiting the reduction of Cu^+ at the surface [121].

Among the above materials, Cu_3VO_4 has the narrowest bandgap energy (1.2 eV) and as a result the highest theoretical maximal photocurrent density (−39.7 mA cm^{-2} under AM1.5). Initial reports of Cu_3VO_4 photocathodes synthesized by solid-state reaction of Cu_2O and V_2O_4 in a vacuum line at 550 °C and then annealed at 400 °C in dynamic vacuum showed relatively low photocurrent densities below −0.1 mA cm^{-2} in 0.5 M Na_2SO_4 (pH 5.8) although cathodic photocurrent started at a relatively positive potential of ~0.72 V versus RHE (0.13 V versus SCE) [122]. Annealing the samples to 350 °C in air oxidized some of the Cu(I) to Cu(II) resulting in Cu_3VO_4 particles being coated with CuO and $Cu_3V_2O_8$ nanorods and improved the photocurrent density to ~ −0.2 mA cm^{-2} at 0.39 V versus RHE (−0.2 V versus SCE).

Many of the Cu(I) niobates ($CuNb_2O_6$, $CuNb_3O_8$, $Cu_2Nb_8O_{21}$, and $CuNbO_3$) have ideal bandgap energies (1.26–2.00 eV) for reaching relatively high J_{max} values (−14.6 to −37.1 mA cm^{-2}) but so far the reported photocurrent densities have been smaller than −1 mA cm^{-2} in aqueous electrolyte solutions at potentials between −0.35 and 0.35 V versus RHE [123–128, 133]. $CuNb_2O_6$ photocathodes were constructed by first synthesizing $CuNb_2O_6$ powders via a solution combustion reaction which were then spray-coated onto ITO substrates [123]. These photocathodes produced a photocurrent density of about −0.15 mA cm^{-2} in 0.1 M $NaHCO_3$ saturated with CO_2 (pH ~ 7) at ~0.16 V versus RHE (~ −0.45 V versus Ag/AgCl). The photocurrent onset occurred at ~0.78 V versus RHE. The group of Maggard prepared $CuNb_3O_8$ photocathodes on FTO substrates from $CuNb_3O_8$ powder synthesized by solid-state reaction of Cu_2O and Nb_2O_5 at 750 °C [124]. The photocathodes reached a photocurrent density of ~ −0.45 mA cm^{-2} in 0.5 M Na_2SO_4 (pH 6.3) at −0.35 V versus RHE. Mott–Schottky analysis showed a flat-band potential of 0.35 V versus RHE and application of the Mott–Gurney equation to *J-V* measurements of pressed pellets revealed a hole mobility of ~145 $cm^2\ V^{-1}\ s^{-1}$. The same group synthesized $Cu_2Nb_8O_{21}$ nanoparticles by ion-exchange solvothermal reaction of CuCl with Li_3NbO_4 nanoparticles. Of the Cu(I) niobates, these $Cu_2Nb_8O_{21}$ have shown the highest photocurrents. After

annealing at 350 and 450 °C they had a cathodic photocurrent onset at about 0.95 V versus RHE (~0 V versus SCE) and reached photocurrent densities of ~ −0.9 mA cm^{-2} in 0.5 M Na_2SO_4 solution (adjusted to pH = 12 with NaOH) at ~0.35 V versus RHE (~ −0.6 V versus SCE) [126]. Most recently, the Maggard group showed results for $CuNbO_3$ photocathodes synthesized by solid-state reaction of Cu_2O and Nb_2O_5 followed by doctor-blading onto FTO substrates. These photocathodes had a flat-band potential of 1.08–1.14 V versus RHE and a photocurrent density of ~ −0.45 mA cm^{-2} in Na_2SO_4 and NaOH (pH 12) at 0.35 V versus RHE (−0.6 V versus SCE) [128]. The discovery of these Cu(I) niobates as photoactive materials is quite recent so there are only few reports on them in the literature. As a result not all of their photophysical properties related to PEC have been established including their absorption coefficients and charge carrier mobilities and diffusion lengths. Although these initial reports show relatively low photo-conversion efficiencies their bandgap energies and relatively positive photocurrent onset potentials make them promising candidates for high efficiency tandem PEC devices. More experiments may help determine whether the low photocurrent density is mainly due to limitations in charge carrier transport, reaction kinetics, or other factors.

The next interesting class of Cu(I) oxides is the tantalates. So far, the Cu(I) tantalates (β-$Cu_2Ta_4O_{11}$, $Cu_3Ta_7O_{19}$, and $Cu_5Ta_{11}O_{30}$) have shown relatively high photocurrent densities—as compared to the vanadates and the niobates—in the range of −1.3 to −2.2 mA cm^{-2} in aqueous electrolyte solutions at potentials near 0.0 V versus RHE [129, 130, 132]. $Cu_3Ta_7O_{19}$, and $Cu_5Ta_{11}O_{30}$ powders were prepared using a molten salt flux method with CuCl as the flux, and further deposited onto FTO as photocathodes using a doctor-blade technique. Various annealing steps were used to treat the films. Mott–Schottky analysis revealed that the $Cu_3Ta_7O_{19}$, and $Cu_5Ta_{11}O_{30}$ photocathodes have flatband potentials of 1.19 and 1.06 V versus RHE, respectively. When annealed in Ar at 500 °C and then oxidized in air at 350 °C, the $Cu_5Ta_{11}O_{30}$ produced a photocurrent density of ~ − 2.2 mA cm^{-2} in 0.5 M Na_2SO_4 at ~ 0 V versus RHE (−0.6 V versus SCE at pH 6.3). Like the Cu(I) niobates, the Cu(I) tantalates are relatively new materials for PEC and not all of the relevant PEC properties have been established. These materials may be capable of reaching high quantum efficiencies; however, one significant limitation is their moderate bandgap energy (2.55–2.65 eV) which limits J_{max} to −4.5 to −5.6 mA cm^{-2} under AM1.5. Even if they can be optimized to achieve nearly 100% quantum yield, their solar-to-hydrogen efficiency will remain below 10%, which is the current state of $BiVO_4$ ($E_g \approx 2.4$ eV) after thorough optimization as an n-type photoanode material.

4.2.1.3. Cu(I) delafossites. Copper(I) delafossites have the general formula of $CuMO_2$, in which M is a metal cation in the +3 oxidation state (M = Al, Co, Cr, Fe, Ga, In, La, Sc, Y) [121, 134–136]. Their predominant crystal structure consists of alternating layers of close-packed Cu^+ cations and edge-shared MO_6 octahedra with each oxygen coordinated by one Cu^+ and three M^{3+} cations [134]. They can crystallize in either a rhombohedral 3R- ($R\bar{3}m$) or hexagonal 2H- ($P6_3/mmc$) polymorph. The optical bandgap energy of delafossites can vary widely (1.36–4.15 eV) depending on which +3 metal cation is present [135–137]. This has led to delafossites being used for a variety of applications including dye-sensitized solar cells, absorber layers in PV and PEC devices, and transparent p-type conducing oxides (TCOs) [121].

Among the Cu(I) delafossites, $CuFeO_2$, a p-type metal oxide, is particularly attractive as a photocathode material because it has an ideal optical bandgap (1.36–1.55 eV) and it is composed of abundant elements [138–140]. It has a conduction band edge of −0.05 to −0.46 V versus RHE, so photogenerated electrons are energetic enough to reduce protons. In addition, it has a relatively positive flatband potential of 0.83–1.3 V versus RHE, making it well suited for a tandem PEC device [138–140]. Based on the bandgap it has relatively high J_{max} value of −30 mA cm^{-2}, but so far the reported values have been much lower in magnitude. A photocurrent density of −1.5 mA cm^{-2} at 0.35 V versus RHE was achieved with O_2 as a sacrificial electron scavenger for layered $CuFeO_2$ thin films synthesized by a sol-gel method [139]. This was obtained after thermal intercalation of oxygen into the layered delafossite structure of the $CuFeO_2$ thin films, which increased both the acceptor density and photocurrent density by similar orders of magnitude. In the presence of O_2 these $CuFeO_2$ photocathodes were stable under illumination in 1 M NaOH for over 40 h. With a protective AZO/TiO_2 overlayer along with photodeposited Pt, they produced a sustained hydrogen production photocurrent density of −0.4 mA cm^{-2} at 0 V versus RHE in 0.5 M Na_2SO_4 (buffered to pH 6.1) [139]. The limited photocurrent density was attributed to poor electron–hole separation so a guest-host strategy was later adopted, in which $CuFeO_2$ was synthesized on top of a nanostructured $CuAlO_2$ scaffold to increase the light absorption of $CuFeO_2$ while minimizing the film thickness and hence the minority carrier charge transport length [141]. The resulting host-guest $CuAlO_2$/$CuFeO_2$ photocathodes increased the photocurrent density to −2.4 mA cm^{-2} at 0.4 V versus RHE in the presence of O_2. Recently, the Lee group explored different annealing treatments of $CuFeO_2$ films including hybrid microwave annealing (HMA), which allowed for rapid heating (above 800 °C in 10 min) causing oxygen intercalation into the crystal lattice [142]. HMA treated $CuFeO_2$ photoelectrodes were combined with NiFe-double layered hydroxide (LDH) and reduced graphene oxide (RGO) as an electrocatalyst overlayer to produce a photocurrent density of −2.4 mA cm^{-2} at 0.4 V versus RHE in Ar-purged NaOH electrolyte.

The recent improvements in $CuFeO_2$ photocathodes to reach −2.4 mA cm^{-2} represents a forward progress, but considerable efforts are still needed to reach the theoretical maximal value of −30 mA cm^{-2}. Further research is needed to isolate the main factors that limit the photocurrent density. Poor electron–hole separation has been suggested as a major limitation. With mobility values of ~0.1 and ~1 × 10^{-6} cm^2 V^{-1} s^{-1} for holes and electrons, respectively, the performance of $CuFeO_2$ might be improved with further optimization of the nanostructure and/or doping [143]. Isolation and passivation of any surface states and traps (recombination centers) may also be implemented.

4.2.1.4. Wide bandgap delafossites. Although they are not well-suited for highly efficient absorber layers because they do not absorb visible light, the wide bandgap delafossites may be useful for PEC applications as p-type TCO layers. The list of delafossites that can be used as p-type TCO materials includes $CuBO_2$ ($E_g \approx 2.2$–4.5 eV) [144, 145], $CuCrO_2$ ($E_g \approx 2.95$–3.30 eV) [146], $CuGaO_2$ ($E_g \approx 2.72$–3.6 eV) [147, 148], $CuInO_2$ ($E_g \approx 3.9$–4.15 eV) [137, 149, 150], $CuScO_2$ ($E_g \approx 3.3$ eV) [151], and $CuYO_2$ ($E_g \approx 3.5$ eV) [152].

4.2.2. Cu(II)-based oxides.

4.2.2.1. CuO. The most simple Cu(II)-based oxide is cupric oxide, CuO, which has a bandgap energy of 1.35–1.7 eV and hence a theoretical maximal photocurrent density of ~28 mA cm^{-2} [105–107, 153]. CuO has a monoclinic crystal structure (space group C2/c, $a = 4.6837$ Å, $b = 3.4226$ Å, $c = 5.1288$ Å, $\beta = 99.548°$, $\alpha = \gamma = 90°$) [107]. It is an antiferromagnetic semiconductor, and the charge carrier mobility is estimated to be relatively low (10^{-2}–10^{-3} cm^2 V^{-1} s^{-1}) as compared to covalent semiconductors, but this is a typical mobility range for metal oxides [154–156]. The flat band potential of CuO is located at 1.21–1.48 V versus RHE, which places the conduction band more negative than 0.0 V versus RHE. Thermodynamically, photogenerated electrons in CuO should therefore be able to reduce protons [153, 157, 158]. However, the electrochemical reduction potential to reduce CuO to Cu_2O is even more positive than the potential to reduce Cu_2O to Cu, which is more positive than 0.0 versus RHE; CuO is just as susceptible to photocorrosion as Cu_2O [112–114, 159]. Several groups have demonstrated photocurrent densities of -2 to -4 mA cm^{-2} at 0 V versus RHE for various CuO photocathodes, but long-term stability were not demonstrated in these early reports and a portion of the photocurrent likely went towards photocorrosion [160–163]. Similar protection layer strategies that have been used for Cu_2O can also be used to stabilize CuO. One group demonstrated photoactivity for CuO nanofibers coated with AZO and TiO_2, but stability measurements were not included in the report [164]. Recently, another group reported that ALD of ZnO and TiO_2 on top of CuO photocathodes significantly reduced the photoactivity; however, chemical bath deposition of CdS followed by ALD of TiO_2 and photodeposition of Pt as a catalyst was effective at stabilizing CuO [165]. These CuO/CdS/TiO_2 photocathodes with Pt maintained a photocurrent density of about -1.25 mA cm^{-2} at 0 V versus RHE for 30 min with a Faradaic efficiency of nearly 1 for H_2 production.

4.2.2.2. $CuBi_2O_4$. $CuBi_2O_4$ is a p-type metal oxide semiconductor with a bandgap energy of 1.6–1.8 eV resulting in a J_{max} of ~20 mA cm^{-2} [1, 158, 166–168]. It has a tetragonal crystal structure (space group (P4/ncc, $a = b = 8.500 - 8.511$ Å, $c = 5.814 - 5.823$ Å, $Z = 4$) consisting of planar CuO_4 complexes stacked along the *c*-axis in a staggered manner with Bi atoms arranged between the stacks and bonded to 6 oxygen atoms by three different bond distances [169–171]. The flatband potential is exceptionally positive at 1.26–1.43 V versus RHE, which results in photocurrent onset >1 V versus RHE [158, 168, 172]. This makes $CuBi_2O_4$ an ideal candidate for the top absorber in a tandem (dual absorber) PEC device [4]. $CuBi_2O_4$ has a relatively low mobility of 10^{-3} cm^2 V^{-1} s^{-1} but the lifetime leads to a carrier diffusion length of 10–52 nm, which is reasonable for a metal oxide.

$CuBi_2O_4$ was first demonstrated to be photoactive for reduction reactions in 2007 through a combinatorial study by the group of Sayama [166]. Like many of the new Cu containing multinary metal oxides, $CuBi_2O_4$ has not yet shown photocurrent densities near the theoretical limit. Recently the group of Choi prepared $CuBi_2O_4$/Ag–$CuBi_2O_4$ photocathodes using a two-step electrodeposition procedure in which the $CuBi_2O_4$ layer was first deposited in an ethylene glycol solution and the Ag–$CuBi_2O_4$ (Ag doped $CuBi_2O_4$) was deposited using a dimethyl sulfoxide solution [172]. These photocathodes produced a photocurrent density of -1.5 mA cm^{-2} at 0.6 V versus RHE in 0.1 M NaOH saturated with O_2 as an electron scavenger. For undoped $CuBi_2O_4$, we have demonstrated a photocurrent density of around -1 mA cm^{-2} at 0.6 V versus RHE in phosphate buffered K_2SO_4 with H_2O_2 as the electron scavenger [168]. In the presence of electron scavengers the material appears relatively stable. Without electron scavengers the reported photocurrents are much lower, which suggests that one of the problems with the material is its poor catalytic behavior for water reduction. Pt has been deposited on the surface of various $CuBi_2O_4$ photocathodes, resulting in photocurrent densities between -0.5 and -0.6 mA cm^{-2} at 0.6 V versus RHE for N_2 or Ar purged electrolytes [168, 172, 173]. These are much lower than the photocurrents in the presence of electron scavengers, which suggests that although Pt is a well-known electrocatalyst for proton reduction, it may not be ideal when combined with $CuBi_2O_4$. Other catalysts therefore need to be explored.

Even if the catalytic limitation is solved, it is not likely to bring the photocurrent of $CuBi_2O_4$ close to the J_{max}. Perhaps the greatest bottleneck for achieving high photocurrent density with $CuBi_2O_4$ is poor charge carrier transport within $CuBi_2O_4$ films [168]. and possibly at the $CuBi_2O_4$-substrate interface when FTO is used. This suggests that strategies used on other metal oxides such as $BiVO_4$ and Fe_2O_3 may be successful with $CuBi_2O_4$ including nanostructuring and doping. As mentioned previously Ag doping has been used to improve the photoactivity of $CuBi_2O_4$ by improving charge carrier transport. It has also been shown that Ag can be incorporated while remaining in the zero valence state at potentials more positive than 1.0 V versus RHE, which appears to be beneficial towards the reduction reaction kinetics [158]. The $CuBi_2O_4$-FTO interface has also been suggested to be the possible source for photocurrent loss. Other substrates which ideally form Ohmic junction without introducing high density of interface states (e.g. Au, p-TCO) need to be investigated. Finally, another major challenge is the susceptibility to photocorrosion in aqueous electrolyte in the absence of electron scavengers (e.g. O_2, H_2O_2) [168, 172]. Figure 13 shows a clear evidence that copper was reduced from 2+ to 1+ oxidation state at the surface of $CuBi_2O_4$ during photoelectrochemical measurements [168]. Some of the strategies used for Cu_2O and CuO such as ALD protection layers may also be useful with $CuBi_2O_4$.

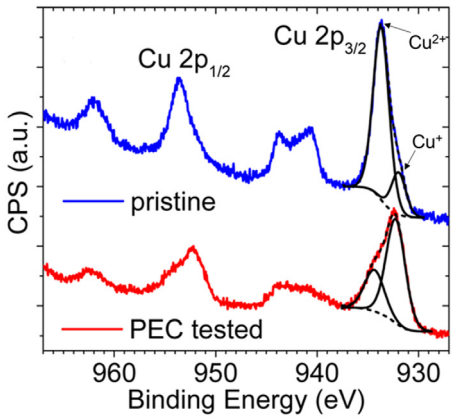

Figure 13. Cu 2*p* core-level x-ray photoelectron spectroscopy (XPS) spectra of $CuBi_2O_4$ photocathode before and after chronoamperometry measurement at 0.6 V versus RHE for 2 h in 0.3 M K_2SO_4 and 0.2 M phosphate buffer (pH 6.65) with Ar bubbling. Adapted with permission from Berglund *et al* [168]. Copyright 2016 American Chemical Society.

4.2.3. Metal tungstates. Several metal tungstates with appropriate bandgaps have been investigated as a photoelectrode material. Among them, copper tungstate ($CuWO_4$) is one of the more well-studied materials, with reports on $CuWO_4$ photoelectrodes dating back to more than 30 years ago [174]. This material was recently revisited in the last 5 years; a number of researchers reported the fabrication of thin films of $CuWO_4$ and measured the photoelectrochemical behavior [175–182]. $CuWO_4$ has a triclinic crystal structure (space group $P\bar{1}$ with $a = 4.7026$ Å, $b = 5.8389$ Å, $c = 4.8784$ Å, $\alpha = 91.677°$, $\beta = 92.469°$, $\gamma = 82.805°$), similar to monoclinic wolframite with an added Jahn–Teller distortion of Cu^{2+} [183–186]. As shown in figure 14(a), both Cu and W ions are coordinated octahedrally with six O atoms; Cu and W form alternating sequence of layers between the oxygen sheets. The crystalline phase is typically an n-type semiconductor, while p-type conductivity has been reported in amorphous $CuWO_4$ [180]. Initial studies reported conflicting bandgap values of 1.5 and 3.5 eV [187, 188], yet recent thin film studies have consistently shown an indirect bandgap value of ~2.2 eV [175–178].

The photoelectrochemical performance is limited by two factors. First, charge transfer between the surface and the electrolyte is inefficient [179, 182]. Interestingly, this issue seems to be not easily solved by depositing an oxygen evolution co-catalyst (OEC) layer, possibly due to the presence of large density of midgap states at the surface of $CuWO_4$ [175]. An even bigger limitation is the charge carrier transport within the material. Although a high hole mobility of 100 cm^2 V^{-1} s^{-1} has been reported for a single-crystal $CuWO_4$ [189], the value for the polycrystalline thin films are likely to be much smaller. This is evident from the reported bulk resistance in the order of 3 kΩ cm^{-2} [180]. Certain strategies, such as doping [182] and composite formation with multiwall carbon nanotubes [181], have been implemented to address this issue; yet, more than 92% of the carriers still recombine before they reach the interface or surface. Future efforts should be focused on overcoming these two limitations, e.g. fabricating a nanostructured film with feature sizes smaller than the carrier diffusion length. Fundamental studies on the carrier transport properties are therefore also needed to direct this effort.

Another possible candidate in the metal tungstate class is iron tungstate (Fe_2WO_6). It has an orthorhombic crystal structure (space group Pbcn, $a = 4.576$ Å, $b = 16.766$ Å, $c = 4.967$ Å), as shown in figure 14(b). Fe and W atoms are each coordinated with eight oxygen atoms (octahedral), which form zigzag chains along the *c*-axis. Fe_2WO_6 is typically n-type [190, 191], although it has to be mentioned that reports on this material are very limited. One particular property stands out, which is the attractive bandgap of ~1.5–1.7 eV [190, 192]. Unfortunately, other properties of the material do not seem to be very attractive. The flatband potential is relatively unfavorable at ~0.6–0.7 V versus RHE, and the carrier concentration is in the range of 10^{19}–10^{20} cm^{-3}, even after high temperature treatment at 800 °C [193]. As a result, the photocurrent remained modest, and charge separation efficiency of only 5% was reported [193, 194]. This may be related to the reported drift mobility of 4.7×10^{-4} cm^2 V^{-1} s^{-1}, attributed to the small polaron conduction mechanism [192]. Although it seems to be unlikely, these challenges need to be overcome for Fe_2WO_6 to be a suitable photoelectrode material.

Tin tungstate ($SnWO_4$) is also interesting as a photoelectrode material. It has two crystal structures. The first is β-$SnWO_4$, which has a cubic crystal structure and large bandgap of ~4.1 eV [195, 196]. This structure is stable above 670 °C, and can be obtained by rapid quenching following calcination above this temperature [197]. The more interesting polymorph is α-$SnWO_4$ (see figure 14(c)), with orthorhombic crystal structure (space group Pnna, $a = 5.625$ Å, $b = 11.744$ Å, $c = 4.986$ Å) [195]. The bandgap is reported to be ~1.5–1.6 eV, indirect in nature, but still possess relatively high absorption coefficient (~10^5 cm^{-1}) [195, 198]. Theoretically, a maximum AM1.5 photocurrent of close to 30 mA cm^{-2} is possible with α-$SnWO_4$. It has an n-type conductivity, and the carrier mobility is expected to be relatively high. Although there is no experimental report on the transport properties, a DFT calculation shows band structures with relatively large curvature (figure 15); an effective mass of electrons and holes of 0.35 and 0.8, respectively, were reported [198]. As a comparison, values of 0.9 and 0.7 were calculated for the effective masses of electron and holes in $BiVO_4$, respectively [26]. The transport was expected to be anisotropic, with effective masses of electrons and holes being the lowest in the [100] and [0 0 1] direction, respectively. The flatband potential has been estimated through Mott–Schottky analysis to be −0.1–0.0 V versus RHE [198, 199]. This implies that the band positions nicely straddle the hydrogen and oxygen evolution potentials, and only little (or no) overpotential is needed to generate the water splitting reaction. However, the AM1.5 photocurrents are still relatively low, with the highest reported value of ~0.3 mA cm^{-2} at 1.23 V versus RHE (~1% of the theoretical maximum) [198]. The exact cause of the low photocurrent is not clear. One possibility is the high carrier density observed in these reported films (~10^{20} cm^{-3}), which can often be correlated to the presence of defects that may act as recombination centers. Implementing strategies that may reduce these

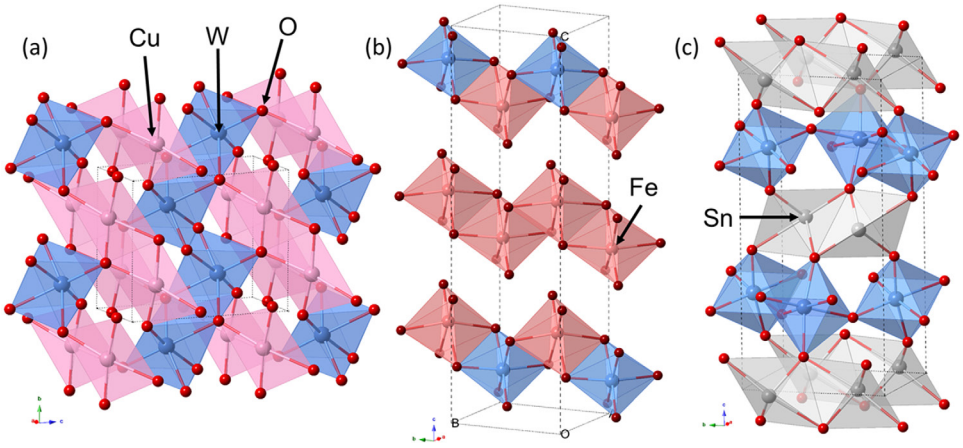

Figure 14. Crystal structure of (a) triclinic $CuWO_4$, (b) orthorhombic Fe_2WO_6, and (c) orthorhombic $SnWO_4$.

defects (e.g. heat treatment, dopant compensation) therefore potentially improves the photocurrent. Another limitation of the material is related to its chemical stability. Sn^{2+} easily oxidizes to Sn^{4+}, and acts as a potential trap site for electrons [198, 200, 201]. Protection layer strategies (using e.g. TiO_2, NiO_x) should be explored in order to address this issue.

4.2.4. Metal vanadates. Other than $BiVO_4$, several metal vanadates have been extensively investigated as photocatalysts. These include yttrium vanadate (YVO_4) and indium vanadate ($InVO_4$) [202–205]. However, these vanadates possess an even larger bandgap as compared to $BiVO_4$. One of the smaller bandgap metal vanadates is iron vanadate ($FeVO_4$), with a bandgap of ~2.0 eV [206, 207]. Figure 16(a) shows the triclinic crystal structure (space group $P\bar{1}$, $a = 6.7794$ Å, $b = 8.0937$ Å, $c = 9.3931$ Å, $\alpha = 96.434°$, $\beta = 106.572°$, $\gamma = 101.56°$) [208], consisting of iron octahedral (FeO_6) and vanadium tetrahedral (VO_4). An early study suggested that small polaron hopping is the conduction mechanism below 500 K, and a hole mobility of 10^{-2} $cm^2\,V^{-1}\,s^{-1}$ was estimated [209]. This study seemed to suggest that $FeVO_4$ has p-type conductivity, however, more recent reports on $FeVO_4$ films show only n-type behavior [206, 207, 210]. Donor-type doping with W has also been reported to improve the performance of $FeVO_4$ [207]. AM1.5 photocurrents in the range of ~0.1 mA cm^{-2} have been reported, which seems to be limited by the poor carrier transport properties. In our lab, we have attempted to directly measure the carrier lifetime in spray-pyrolysed $FeVO_4$ using time-resolved microwave conductivity (TRMC). The preliminary measurements, however, show no signal, which means that the carrier lifetime is shorter than ~10 ns. Combined with the low carrier mobility, this suggests a rather short carrier diffusion length (<20 nm). Nanostructuring efforts should therefore be employed in order to overcome this limitation.

It should also be noted that other stoichiometries of iron vanadate with desirable bandgaps (<2.0 eV) have been reported (e.g. FeV_2O_4, Fe_2VO_4, $Fe_2V_4O_{13}$) [210, 211], but very limited reports are available in terms of the PEC and optoelectronic properties. Some of these structures may also be interesting as a possible candidate for photoelectrode materials.

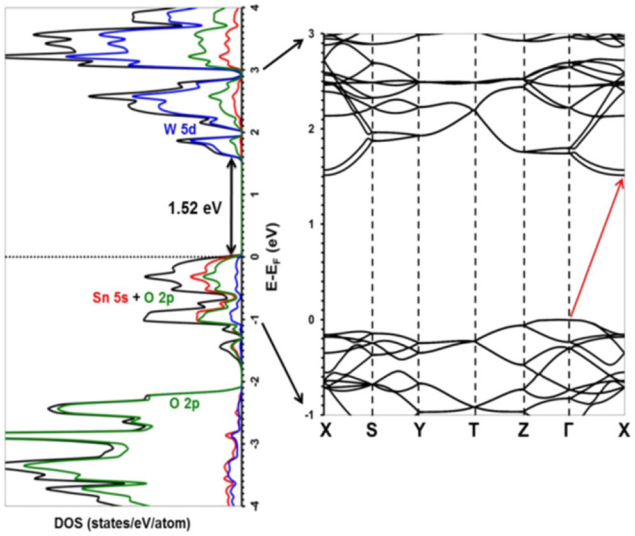

Figure 15. Density of states (DOS) calculation for the orthorhombic tin tungstate (α-$SnWO_4$). Reprinted with permission from Harb *et al* [195] John Wiley & Sons. © 2016 WILEY-VCH Verlag GmbH & Co. KGaA, Weinheim. Left: total DOS is shown in in black, DOS projected on Sn 5*s* orbitals in red, on W 5*d* orbitals in blue, and on O 2*p* orbitals in green. The Fermi level is set at 0 eV. Right: DOS projected onto the *k*-space of $SnWO_4$.

High throughput experiments and calculations have been performed on metal vanadates [212, 213]. One of the resulting hits is manganese pyrovanadate (β-$Mn_2V_2O_7$). It has a monoclinic crystal structure (space group C2/m, $a = 6.713$ Å, $b = 8.725$ Å, $c = 4.969$ Å, $\beta = 103.591°$) [212]. The structure is composed of edge-sharing MnO_6 octahedra brought together by V_2O_7 bi-tetrahedra, as shown in figure 16(b). It has been reported to be paramagnetic at room temperature, which transforms to be antiferromagnetic at low temperature (~20 K) [214, 215]. Similar to $BiVO_4$, the conduction band is composed of mainly V 3*d* orbitals. The valence band is hybridized Mn 3*d* and O 2*p* orbitals, which brings the valence band maximum upward [212, 216]. As a result, it has a desirable bandgap of ~1.75 eV, and the band positions have been reported to (closely) straddle the oxygen and hydrogen evolution potential [212, 216]. No photocurrent was however reported for water oxidation; a small photocurrent was only

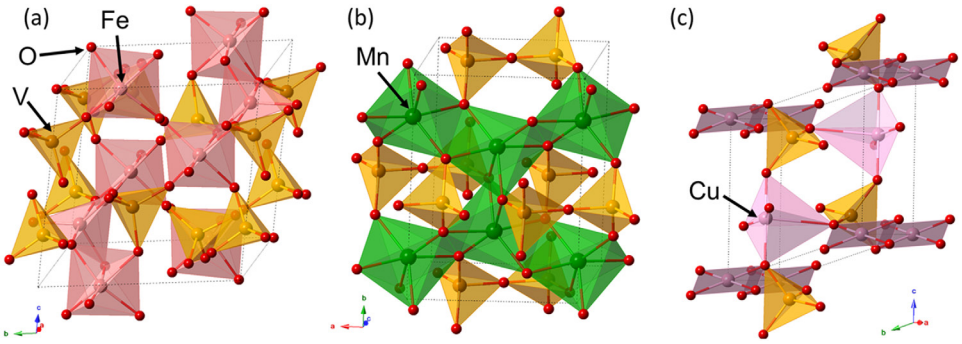

Figure 16. Crystal structure of (a) triclinic $FeVO_4$, (b) monoclinic $Mn_2V_2O_7$, and (c) monoclinic $Cu_3V_2O_8$.

observed when a facile redox couple is present in the electrolyte [212]. It has been argued that this may be caused by the relatively small overpotential between the valence band edge and the oxygen evolution potential (~0.3 V), and applying appropriate oxygen evolution co-catalyst on the surface of β-$Mn_2V_2O_7$ may solve the problem. An additional limitation has, however, been identified in our lab. TRMC measurement on β-$Mn_2V_2O_7$ revealed a very small mobility of ~10^{-4} $cm^2\ V^{-1}\ s^{-1}$, which may prevent the photogenerated charge carriers from reaching the surface or interface.

Another system that has been investigated through high-throughput experimentation is the copper vanadate system. Although copper vanadate compounds have been identified since ~60 years ago [217–224], they were mostly considered for the applications in phase change materials and Li-ion batteries. It was not until very recently that the system was considered for photoelectrode materials [213, 225–229]. Zhou *et al* explored large stoichiometries in the CuO–V_2O_5 system using their high-throughput experiments and computations [213]. They discovered four major phases in their compositional library: Blossite (α-$Cu_2V_2O_7$), Ziesite (β-$Cu_2V_2O_7$), McBirneyite (γ-$Cu_3V_2O_8$), and Fingerite ($Cu_{11}V_6O_{26}$). All were reported to be n-type semiconductors with bandgap in the range of 1.8–2.0 eV [213, 225–228]. Among these, γ-$Cu_3V_2O_8$ seems to be currently the most promising candidate. The crystal structure of γ-$Cu_3V_2O_8$ is shown in figure 16(c); V is tetrahedrally coordinated (VO_4), while Cu is present in both square-planar (CuO_4) and square-pyramidal (CuO_5) coordination. Charge transfer across the semiconductor/electrolyte interface has been identified as one of the PEC limitation, with the photocurrents in the presence of hole scavengers to be a factor of ~3 higher than the water oxidation photocurrents [226]. Quantum efficiencies in the range of 5–10% have also been reported [213, 226], which is promising considering the early stage of the photoelectrode material development. Seabold *et al* estimated the diffusion length to be ~100 nm, and donor-doping with Mo seems to increase the diffusion length to be ~450 nm [226]. The stability of γ-$Cu_3V_2O_8$ is excellent in the pH 9.2 borate buffer electrolyte [213, 226, 228], which was proposed to be caused by self-passivation of the surface due to the complexation with the borate electrolyte. Corrosion/degradation was reported for γ-$Cu_3V_2O_8$ in other pHs (6–7 and 10–14) and electrolytes (phosphate, sulfate, carbonate, nitrate, and hydroxide) [226]. This narrow stability window is very interesting; further investigation in revealing the specificity of pH 9 or borate in the electrolyte may be found to be very useful in the efforts of improving the stability of photoelectrode materials beyond γ-$Cu_3V_2O_8$. An additional challenge for the material is the relatively positive flatband potential of ~0.6–0.7 V versus RHE [226]. This means that relatively high bias potential would need to be applied for water oxidation, and γ-$Cu_3V_2O_8$ needs to be combined with a tandem material which has a relatively large photovoltage.

4.2.5. Spinels. Spinels are a class of metal oxides with the general formula of AB_2O_4 in which A and B are metal cations with oxidations states of +2 and +3, respectively. For some spinels A and B can be of the same element (e.g. Fe_3O_4). The majority of spinel compounds crystallize in the cubic crystal system (space group *Fd3m*) with the oxygen anions arranged in pseudo-cubic close-packed (ccp) lattice and the A and B cations occupying tetrahedral and octahedral sites [230]. The flexible crystal structure of spinels leads to a wide range of material properties and applications [231]. Perhaps the most commonly studied spinels for PEC are $CaFe_2O_4$ and $ZnFe_2O_4$, which will be described in more detail later. Other spinels that can potentially be employed as photoelectrodes include $CuCr_2O_4$ ($E_g \approx 1.4$ eV) [232], $CuAl_2O_4$ ($E_g \approx 2.1$ eV) [233], $CuCo_2O_4$, $CuFe_2O_4$ ($E_g \approx 1.80$–2.03 eV) [234], $CuMn_2O_4$, $FeCr_2O_4$ ($E_g \approx 1.33$ eV) [235], and $NiFe_2O_4$ ($E_g \approx 1.56$ eV) [236]. The Trari group showed that these spinels can photocatalytically evolve hydrogen when suspended as powders in solutions containing sacrificial reagents (S^{2-}, SO_3^{2-}, or $S_2O_3^{2-}$) as hole scavengers [232, 233, 235]. These spinels have ideal bandgap energies for producing high photocurrent densities, but limited photoelectrode reports are available. Other spinels such as $NiFe_2O_4$ ($NiFe_2O_x$), $NiCo_2O_4$ ($NiCo_2O_x$), and $CoGa_2O_4$ have been reported to be highly active in the dark as electrocatalysts for the oxygen evolution reaction [237–240]. They therefore may be suitable to be combined as co-catalysts with certain photoanodes.

4.2.5.1. $CaFe_2O_4$. Cuprospinel, $CaFe_2O_4$, is a p-type semiconductor, which has been tested as a photocathode. It has a bandgap energy of 1.9 eV ($J_{max} \approx 17$ mA cm^{-2}) and the conduction and valence band edges are located at −0.6 and 1.3 V versus RHE, respectively, so it should be able to reduce protons under illumination [241, 242]. $CaFe_2O_4$ photocathodes prepared by calcination of $CaFe_2O_4$ powder onto a Pt substrate had a photocurrent onset potential of 1.22 V versus RHE (0.31 V versus

Ag/AgCl) in 0.1 M NaOH and reached a photocurrent density of ~ − 1 mA cm^{-2} at 0.11 V versus RHE (−0.8 V versus Ag/AgCl) [242]. When the photocathode was paired with a TiO_2 photoanode in a two-electrode configuration, H_2 was produced spontaneously without additional applied potential. Since then the quantum efficiency of $CaFe_2O_4$ photoelectrodes have not been improved significantly. Charge carrier transport may be a limiting factor. The mobility of $CaFe_2O_4$ has not been reported, but $CaFe_2O_4$ pellets showed conductivity values that were 2–3 orders of magnitude lower than $Ca_{1-x}Na_xFe_2O_4$ pellets ($x = 0.02$, 0.05, 0.2, or 0.4), which had mobility values in the range of 10^{-2}–10^{-1} cm^2 V^{-1} s^{-1} [243]. Electrical impedance spectroscopy (EIS) was used to demonstrate that most photogenerated carriers in $CaFe_2O_4$ photoelectrodes recombined within the bulk of the material rather than reaching the electrolyte surface [244]. Doping $CaFe_2O_4$ with Ag, Na, and Mg has been shown to increase photocurrent density under various illumination sources although the quantum efficiency remained relatively low (IPCE < 3%) [243, 245]. An alternative approach to using $CaFe_2O_4$ has been to combine it with n-type metal oxides such as n-TaON and n-Fe_2O_3 forming heterojunction photoanodes resulting in anodic photocurrent densities up to ~1.6 mA cm^{-2} at 1.6 V versus RHE [246, 247].

4.2.5.2. $ZnFe_2O_4$. $ZnFe_2O_4$ is an n-type semiconductor with a bandgap energy of 1.9–2.1 eV resulting in a J_{max} of ~14.5 mA cm^{-2} [248, 249]. It has been explored as an alternative to α-Fe_2O_3 because hybridization of the Zn 3*d* states shifts the valence band 0.2 V more negative relative to the valance band of α-Fe_2O_3, which could potentially lead to an earlier photocurrent onset potential [249–251]. Mott–Schottky measurements place the flatband potential of $ZnFe_2O_4$ at 0.51–0.64 V versus RHE, compared to 0.75 V versus RHE for α-Fe_2O_3 [252, 253]. Both α-Fe_2O_3 and $ZnFe_2O_4$ show mobility values on the order of ~0.1 cm^2 V^{-1} s^{-1} [254–256]. Unfortunately, most reports on $ZnFe_2O_4$ have not shown it reaching its full potential in regards to photocurrent onset potential and photocurrent density. $ZnFe_2O_4$ thin films deposited by aerosol-assisted chemical vapor deposition (AACVD) showed a flatband potential of 0.83 V versus RHE (−0.17 V versus Ag/AgCl) and a photocurrent density of −350 μA cm^{-2} at ~1.23 V versus RHE. Recently, the Lee group has prepared $ZnFe_2O_4$ nanorod photoanodes by converting β-FeOOH nanorods to $ZnFe_2O_4$ with annealing and etching techniques to remove excess ZnO [248, 257]. Then post treatments were performed such as annealing under air, vacuum, or hydrogen to control oxygen vacancies or hybrid microwave annealing. The resulting $ZnFe_2O_4$ nanorod photoanodes showed significantly higher photoactivity than the control films, but the photocurrent densities were still on the order of 300 μA cm^{-2} at ~1.23 V versus RHE. Recently, the kinetics of water oxidation by $ZnFe_2O_4$ films prepared by atomic layer deposition was measured using intensity modulated photocurrent spectroscopy [253]. The photocurrent onset potential of $ZnFe_2O_4$ was confirmed to be 0.2 V versus RHE more negative than that of α-Fe_2O_3 and the charge transfer efficiency was considerably higher between 0.8 and 1.3 V versus RHE; however, the net photocurrent density was much lower than for α-Fe_2O_3.

5. Combinatorial approaches in the discovery of novel complex metal oxides

As mentioned above, the vast material possibilities within the class of complex metal oxides represent a major challenge in finding the desired photoelectrode material. We therefore need to come up with a methodology to screen various materials with as little time as possible. Combinatorial chemistry has been used to address this challenge. It was first applied in the field of photocatalysis and PEC in 2001 by the group of Maier [258]. Since then a variety of combinatorial approaches have been used in the fields of photocatalysis and photoelectrochemistry [158, 259]. The Parkinson group has consistently used a combinatorial approach in searching for new multinary metal oxides to use as photoelectrodes starting with Al, Co, Cu, and/or Fe spinel type oxides [11, 260, 261]. They showed that $Co_{3-x-y}Al_xFe_yO_4$ (where x and y are about 0.18 and 0.30, respectively) is a p-type semiconductor with an indirect bandgap of 1.5 eV and a photocurrent onset potential around 0.9 eV [260]. Later arrays of $Co_{3-x}M_xO_4$ [M = (Al, Ga, In)] were tested while varying the amount of Co (x) and the Al:Ga:In ratio [262]. The highest photocurrent relative to Co_3O_4 was achieved for Al:Ga:In ratios of ~1.5:1:1.9. Most recently, Fe–Cr–Al containing oxides were synthesized by magnetron sputtering and by scanned using an automated optical scanning droplet cell [263]. Based on the scanning results a larger macroporous photocathode composed of $Fe_{0.84}CrAl_{0.16}O_3$ ($E_g \approx 1.4$ eV, $J_{max} \approx -20$ mA cm^{-2}) was synthesized by sol-gel to test in more detail [264]. It had a photocurrent onset potential of 1.1 V versus RHE and after optimization reached a photocurrent density of −0.68 mA cm^{-2} at 0.5 V versus RHE under AM 1.5 illumination.

The Joint Center for Artificial Photosynthesis (JCAP) has also recently made progress in the combinatorial screening of electrocatalysts and photoelectrodes [265–271]. Arrays of (Ni–La–Co–Ce)O_x and (Ni–Fe–Co–Ce)O_x coatings on $BiVO_4$ were screened with anodic sweeps [266, 267]. In 0.1 M NaOH (pH 13), $La_{0.2}Co_{0.2}Ce_{0.6}O_x$/$BiVO_4$ and $Fe_{0.5}Ce_{0.5}O_x$/$BiVO_4$ photoelectrodes showed a photocurrent onset potentials of 0.42 and 0.43 V versus RHE, respectively. They also screened (Cu–V)O_x system and reported α-$Cu_2V_2O_7$, β-$Cu_2V_2O_7$, γ-$Cu_3V_2O_8$, and $Cu_{11}V_6O_{26}$ as potential absorber materials for photoelectrodes as described in the Metal Vanadates section above [213].

One major challenge of these combinatorial approaches is in determining the criteria in searching the potential candidates. Photocurrent at specific applied potential is probably the easiest parameter to screen. However, this may not be the ideal, since photocurrent is a convoluted parameter affected by the many key properties of the material and as a result promising candidate materials may be missed. It is arguably more useful to screen the potential candidates using their intrinsic properties, such as absorption coefficient, band positions, charge carrier mobility and diffusion lengths, surface reaction kinetics, and photoelectrochemical stability. Combinatorial experimental methods need to be further developed in this direction, although some efforts have indeed been initiated. High throughput efforts in theory (such as DFT calculation of

Table 2. Key material properties of the metal oxides discussed in this topical review.

Material	E_g (eV)	m_{eff}	μ ($cm^2 V^{-1} s^{-1}$)	L_D (nm)	α^{-1} (nm)	V_{FB} (V versus RHE)	Highest reported photo-current (mA cm^{-2})	Refs
n-$BiVO_4$	2.4–2.5	0.9 m_0 (m_e) 0.7 m_0 (m_h)	~0.02 ~0.2 (μ_e, single crystal)	70–100	~100 ($\lambda = 450$ nm)	~0.0	6.7 (1.23 V versus RHE)	[20, 26, 28, 44, 47, 50, 66]
n-$CuWO_4$	2.2–2.4		100 (μ_h)		~500 ($\lambda = 450$ nm)	~0.4	0.25 (1.23 V versus RHE)	[174, 179–182, 189]
n-Fe_2WO_6	1.5–1.7	10 m_0 (m_h)	4.7×10^{-4}	<10	~1000 ($\lambda = 450$ nm)	0.6–0.7	0.25 (1.45 V versus RHE)	[192, 193]
n-$SnWO_4$	1.5–1.6	0.36 m_0 (m_e) 0.8 m_0 (m_h)			~70 ($\lambda = 450$ nm)	−0.1–0.0	0.3 (1.23 V versus RHE)	[195, 198, 199]
n-$FeVO_4$	2.0		10^{-2} (μ_h) 68 (μ_h @ $T > 500$ K)	<20	>1000 ($\lambda = 450$ nm)	~0.5	0.1 (1.23 V versus RHE)	[206, 207, 209, 210]
n-$Mn_2V_2O_7$	1.75	1.34 m_0 (m_e) 0.81 m_0 (m_h)	~10^{-4}		~400 ($\lambda = 450$ nm)		0.1 (0.36 V versus NHE, $[Fe(CN)_6]^{3-/4-}$)	[212]
n-$Cu_3V_2O_8$	1.8–2.0			~100 ~450 (Mo-doped)	~200 ($\lambda = 450$ nm)	~0.6–0.7	0.05 (1.6 V versus RHE)	[213, 226]
n-Fe_2O_3	2.1		0.1 (μ_e @ 1200 K) 0.2 (μ_h @ 1400 K)		~50 ($\lambda = 450$ nm)	~0.7	5.7 (1.23 V versus RHE)	[250, 253, 256, 274, 275]
n-$ZnFe_2O_4$	1.9–2.1		0.07–0.15			0.51–0.64	0.35 (1.23 V versus RHE)	[250, 252–255, 276]
p-Cu_2O	1.9–1.2	0.99 m_0 (m_e) 0.58 m_0 (m_h)	60–130		~80 ($\lambda = 450$ nm)	~0.75	−10 (0 V versus RHE)	[105–111, 277, 278]
p-Cu_3VO_4	1.2					~0.72[a]	−0.2 (0.39 V versus RHE)	[122]
p-$CuNb_2O_6$	1.9					~0.78[a]	−0.15 (0.16 V versus RHE)	[123]
p-$CuNb_3O_8$	1.26		~145 (μ_h)			~0.35	−0.45 (−0.35 V versus RHE)	[124, 125]
p-$Cu_2Nb_8O_{21}$	1.43					~0.95[a]	−0.9 (0.35 V versus RHE)	[126]
p-$CuNbO_3$	2.0				~500 ($\lambda = 450$ nm)	1.08–1.14	−0.45 (0.35 V versus RHE)	[127, 128, 133]
p-α-/β-$Cu_2Ta_4O_{11}$	2.65							[129]
p-$Cu_3Ta_7O_{19}$	2.60					1.19	−1.3 (0 V versus RHE)	[130, 131]
p-$Cu_5Ta_{11}O_{30}$	2.55				~500 ($\lambda = 450$ nm)	1.06	−2.2 (0 V versus RHE)	[130–133]
p-$CuFeO_2$	1.36–1.55		~0.1 (μ_h) ~10^{-6} (μ_e)		~80 ($\lambda = 550$ nm)	0.83–1.30	−2.4 (0.4 V versus RHE)	[138–142]
p-CuO	1.35–1.7	0.78 m_0 ($m_{h,l}$) 3.52 m_0 ($m_{h,t}$) 1.87 m_0 ($m_{h,ave}$)[b]	10^{-2}–10^{-3}		~40 ($\lambda = 450$ nm) ~80 ($\lambda = 550$ nm)	1.21–1.48	−4 (0 V versus RHE)	[105–107, 153–158, 160]
p-$CuBi_2O_4$	1.6–1.8		~10^{-3}	10–52	~250 ($\lambda = 550$ nm)	1.26–1.43	−1.5 (0.6 V versus RHE)	[158, 166–168, 172]
p-$CaFe_2O_4$	1.9					1.22[a]	−1 (0.11 V versus RHE)	[241, 242]
p-$Fe_{0.84}CrAl_{0.16}O_3$	1.8					1.1	−0.68 at (0.5 V versus RHE)	[264]

[a] VFB values are estimated from the photocurrent onset potentials.
[b] Non-isotropic effective masses, different values for longitudinal (l) and transversal (t) directions.

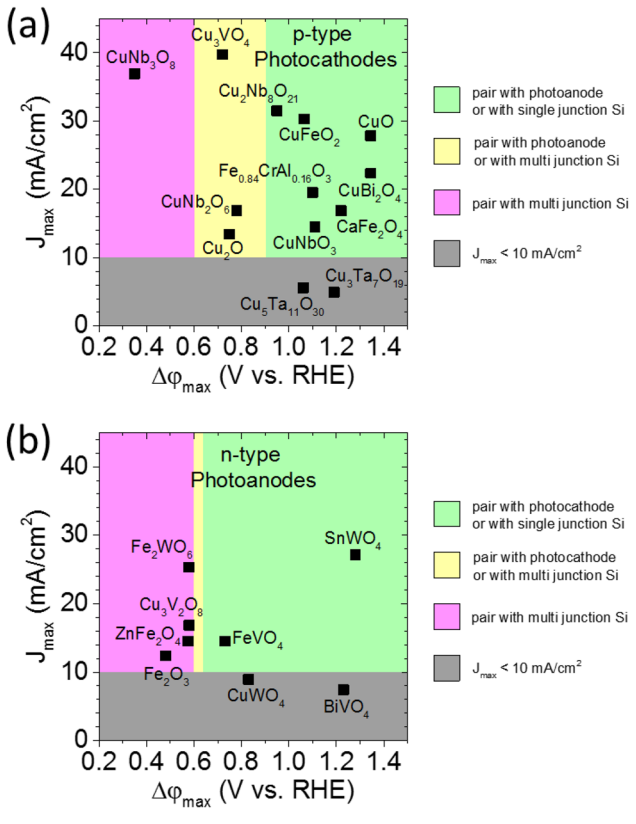

Figure 17. Comparison of the J_{max} and $\Delta\varphi_{max}$ values for (a) p-type photocathode and (b) n-type photoanode materials. Regimes with different colors represent different categories. Grey indicates photocurrent maximum lower than 10 mA cm^{-2}. Green, yellow and magenta differentiate the most suitable tandem configuration for the material.

material libraries) have also been used, and need to be further developed, to help identify promising complex metal oxides [8, 208, 272, 273]. In the end, there needs to be a synergy and a constant feedback mechanism between these experimental and theoretical efforts to expedite the material discovery.

6. Summary

In summary, this topical review has discussed numerous complex metal oxide materials that are potential candidates to be used as photoelectrodes in a PEC water splitting system. Using $BiVO_4$ as a case study it is shown that high efficiencies are possible with metal oxides. However, alternative metal oxides with higher theoretical maximal photocurrent densities must be developed in the same manner to obtain high efficiencies. Discrepancies between the currently observed and theoretical photocurrents are caused by various limitations, as already described in each sections above (e.g. poor carrier separation and surface state recombination for $CuFeO_2$, slow charge transport and non-ideal substrate interface for $CuBi_2O_4$, bulk recombination for $CuWO_4$ and Fe_2WO_6, self-oxidation for $SnWO_4$). Unfortunately, the materials limitations for some of the more novel complex metal oxides—such as the novel Cu(I) complex oxides and metal vanadates—are currently unknown due to lack of reported studies. Efforts are therefore needed to determine the key properties of these materials. The reported properties of the metal oxides discussed in this review are summarized in table 2.

Many of the metal oxides discussed in this review are plotted in figure 17, which includes their J_{max} and $\Delta\varphi_{max}$ values (see Introduction for their definitions). Within each plots of figure 17, the 'green' category represents a promising category, where the theoretical achievable photocurrent is large enough (>10 mA cm^{-2}) and a tandem combination with a simple single-junction solar cell or another ideal photoelectrode would be sufficient. For the p-type photocathodes (figure 17(a)), many metal oxides fall within the promising 'green' category, where high efficiencies can be expected when combined with a simple single-junction silicon solar cell. The challenge is now to improve the achieved photocurrent closer to the theoretical maximal value (J_{max}). Based on table 2, many of the important properties of these p-type photocathodes are still unknown. Studies are therefore needed to reveal these intrinsic properties and determine the main limitation of each material. Based on this, strategies that are already outlined in this review need to be further pursued for these p-type metal oxides. The situation is rather different with the n-type photoanodes. Of all the various complex metal oxides discussed here, only two ($FeVO_4$ and $SnWO_4$) fall within the 'green' category. These two metal oxides are still at the very early stage of their developments, and they need to be further investigated. In addition, combinatorial studies as described above need to be concentrated on this class of materials, which will hopefully result in many more discoveries of promising n-type complex metal oxides. Finally, we note that the list of complex metal oxides discussed here is not exhaustive. This topical review is expected to be used as a roadmap towards highly performing complex metal oxide photoelectrodes, which will expedite the pathway towards efficient commercial PEC water splitting devices.

Acknowledgment

Parts of this work are funded by the German Bundesministerium für Bildung and Forschung (BMBF), project 'MeOx4H2' (03SF0478A).

References

[1] Chen Z *et al* 2010 *J. Mater. Res.* **25** 3
[2] Shockley W and Queisser H J 1961 *J. Appl. Phys.* **32** 510
[3] Bolton J R, Strickler S J and Connolly J S 1985 *Nature* **316** 495
[4] Walter M G, Warren E L, McKone J R, Boettcher S W, Mi Q, Santori E A and Lewis N S 2010 *Chem. Rev.* **110** 6446
[5] Bornoz P, Abdi F F, Tilley S D, Dam B, van de Krol R, Graetzel M and Sivula K 2014 *J. Phys. Chem.* C **118** 16959
[6] McCrory C C L, Jung S, Ferrer I M, Chatman S M, Peters J C and Jaramillo T F 2015 *J. Am. Chem. Soc.* **137** 4347
[7] Xu Y and Schoonen Martin A A 2000 *American Mineralogist* vol 85 (McLean, VA: GeoScienceWorld) p 543
[8] Castelli I E, Hüser F, Pandey M, Li H, Thygesen K S, Seger B, Jain A, Persson K A, Ceder G and Jacobsen K W 2015 *Adv. Energy Mater.* **5** 1400915

[9] Seger B, Pedersen T, Laursen A B, Vesborg P C K, Hansen O and Chorkendorff I 2013 *J. Am. Chem. Soc.* **135** 1057
[10] Seger B, Castelli I E, Vesborg P C K, Jacobsen K W, Hansen O and Chorkendorff I 2014 *Energy Environ. Sci.* **7** 2397
[11] Woodhouse M and Parkinson B A 2009 *Chem. Soc. Rev.* **38** 197
[12] Rettie A J E, Chemelewski W D, Emin D and Mullins C B 2016 *J. Phys. Chem. Lett.* **7** 471
[13] Sleight A W, Chen H Y, Ferretti A and Cox D E 1979 *Mater. Res. Bull.* **14** 1571
[14] Zhao Z Y, Luo W J, Li Z S and Zou Z G 2010 *Phys. Lett.* A **374** 4919
[15] Tokunaga S, Kato H and Kudo A 2001 *Chem. Mater.* **13** 4624
[16] Kudo A, Omori K and Kato H 1999 *J. Am. Chem. Soc.* **121** 11459
[17] Roth R S and Waring J L 1963 *Am. Mineral.* **48** 1348
[18] Bhattacharya A K, Mallick K K and Hartridge A 1997 *Mater. Lett.* **30** 7
[19] Cooper J K, Gul S, Toma F M, Chen L, Glans P-A, Guo J, Ager J W, Yano J and Sharp I D 2014 *Chem. Mater.* **26** 5365
[20] Cooper J K, Gul S, Toma F M, Chen L, Liu Y-S, Guo J, Ager J W, Yano J and Sharp I D 2015 *J. Phys. Chem.* C **119** 2969
[21] Ding K, Chen B, Fang Z and Zhang Y 2013 *Theor. Chem. Acc.* **132** 1
[22] Ding K, Chen B, Fang Z, Zhang Y and Chen Z 2014 *Phys. Chem. Chem. Phys.* **16** 13465
[23] Payne D, Robinson M, Egdell R, Walsh A, McNulty J, Smith K and Piper L 2011 *Appl. Phys. Lett.* **98** 212110
[24] Wadnerkar N and English N J 2013 *Comput. Mater. Sci.* **74** 33
[25] Walsh A, Yan Y, Huda M N, Al-Jassim M M and Wei S H 2009 *Chem. Mater.* **21** 547
[26] Zhao Z Y, Li Z S and Zou Z G 2011 *Phys. Chem. Chem. Phys.* **13** 4746
[27] Kudo A, Ueda K, Kato H and Mikami I 1998 *Catal. Lett.* **53** 229
[28] Sayama K, Nomura A, Arai T, Sugita T, Abe R, Yanagida M, Oi T, Iwasaki Y, Abe Y and Sugihara H 2006 *J. Phys. Chem.* B **110** 11352
[29] Chatchai P, Murakami Y, Kishioka S Y, Nosaka A Y and Nosaka Y 2008 *Electrochem. Solid State Lett.* **11** H160
[30] Galembeck A and Alves O 2000 *Thin Solid Films* **365** 90
[31] Abdi F F, Firet N and van de Krol R 2013 *ChemCatChem* **5** 490
[32] Abdi F F and van de Krol R 2012 *J. Phys. Chem.* C **116** 9398
[33] Zhong D K, Choi S and Gamelin D R 2011 *J. Am. Chem. Soc.* **133** 18370
[34] Berglund S P, Flaherty D W, Hahn N T, Bard A J and Mullins C B 2011 *J. Phys. Chem.* C **115** 3794
[35] Kim T W and Choi K-S 2014 *Science* **343** 990
[36] Seabold J A and Choi K S 2012 *J. Am. Chem. Soc.* **134** 2186
[37] Hong S J, Lee S, Jang J S and Lee J S 2011 *Energy Environ. Sci.* **4** 1781
[38] Ma Y, Kafizas A, Pendlebury S R, Le Formal F and Durrant J R 2016 *Adv. Funct. Mater.* **26** 4951–60
[39] Rettie A J, Chemelewski W D, Lindemuth J, McCloy J S, Marshall L G, Zhou J, Emin D and Mullins C B 2015 *Appl. Phys. Lett.* **106** 022106
[40] Zachäus C, Abdi F F, Peter L M and van de Krol R 2017 *Chem. Sci.* at press (https://doi.org/10.1039/C7SC00363C)
[41] Choi S K, Choi W and Park H 2013 *Phys. Chem. Chem. Phys.* **15** 6499–507
[42] Ding C, Shi J, Wang D, Wang Z, Wang N, Liu G, Xiong F and Li C 2013 *Phys. Chem. Chem. Phys.* **15** 4589
[43] Ye H, Park H S and Bard A J 2011 *J. Phys. Chem.* C **115** 12464
[44] Rettie A J E, Lee H C, Marshall L G, Lin J F, Capan C, Lindemuth J, McCloy J S, Zhou J, Bard A J and Mullins C B 2013 *J. Am. Chem. Soc.* **135** 11389
[45] Kweon K E, Hwang G S, Kim J, Kim S and Kim S 2015 *Phys. Chem. Chem. Phys.* **17** 256
[46] Liu T, Zhou X, Dupuis M and Li C 2015 *Phys. Chem. Chem. Phys.* **17** 23503
[47] Ziwritsch M, Müller S, Hempel H, Unold T, Abdi F F, van de Krol R, Friedrich D and Eichberger R 2016 *ACS Energy Lett.* **1** 888
[48] Jovic V, Rettie A J E, Singh V R, Zhou J, Lamoureux B, Buddie Mullins C, Bluhm H, Laverock J and Smith K E 2016 *Phys. Chem. Chem. Phys.* **18** 31958
[49] Cooper J K, Scott S B, Ling Y, Yang J, Hao S, Li Y, Toma F M, Stutzmann M, Lakshmi K V and Sharp I D 2016 *Chem. Mater.* **28** 5761
[50] Abdi F F, Savenije T J, May M M, Dam B and van de Krol R 2013 *J. Phys. Chem. Lett.* **4** 2752
[51] Sze S M 1981 *Physics of Semiconductor Devices* (New York: Wiley) (https://doi.org/10.1002/0470068329)
[52] Brus L 1984 *J. Chem. Phys.* **80** 4403
[53] Pilli S K, Furtak T E, Brown L D, Deutsch T G, Turner J A and Herring A M 2011 *Energy Environ. Sci.* **4** 5028
[54] Parmar K P S, Kang H J, Bist A, Dua P, Jang J S and Lee J S 2012 *ChemSusChem* **5** 1926
[55] Park H S, Kweon K E, Ye H, Paek E, Hwang G S and Bard A J 2011 *J. Phys. Chem.* C **115** 17870
[56] Abdi F F, Han L, Smets A H M, Zeman M, Dam B and van de Krol R 2013 *Nat. Commun.* **4** 2195
[57] Han L, Digdaya I A, Buijs T W, Abdi F F, Huang Z, Liu R, Dam B, Zeman M, Smith W A and Smets A H 2015 *J. Mater. Chem.* A **3** 4155
[58] Liu C, Li X, Su J and Guo L 2016 *Int. J. Hydrog. Energy* **40** 12705–3330
[59] Srivastav A, Verma A, Banerjee A, Khan S A, Gupta M, Satsangi V R, Shrivastav R and Dass S 2016 *Phys. Chem. Chem. Phys.* **18** 32735
[60] Abdi F F, Dabirian A, Dam B and van de Krol R 2014 *Phys. Chem. Chem. Phys.* **16** 15272
[61] Sang Y, Huang Y, wang W, Fang Z and Geng B 2015 *RSC Adv.* **5** 39651
[62] Cao S-W, Yin Z, Barber J, Boey F Y C, Loo S C J and Xue C 2012 *ACS Appl. Mater. Interfaces* **4** 418
[63] Han L, Abdi F F, van de Krol R, Liu R, Huang Z, Lewerenz H J, Dam B, Zeman M and Smets A H 2014 *ChemSusChem* **7** 2832
[64] Rao P M, Cai L, Liu C, Cho I S, Lee C H, Weisse J M, Yang P and Zheng X 2014 *Nano Lett.* **14** 1099
[65] Shi X, Choi I Y, Zhang K, Kwon J, Kim D Y, Lee J K, Oh S H, Kim J K and Park J H 2014 *Nat. Commun.* **5** 4775
[66] Pihosh Y, Turkevych I, Mawatari K, Uemura J, Kazoe Y, Kosar S, Makita K, Sugaya T, Matsui T and Fujita D 2015 *Sci. Rep.* **5** 11141
[67] Zhou L, Zhao C, Giri B, Allen P, Xu X, Joshi H, Fan Y, Titova L V and Rao P M *Nano Lett.*
[68] Abdi F F, Firet N, Dabirian A and van de Krol R 2012 *MRS Online Proc. Library* **1446** u02–05
[69] Toma F M, Cooper J K, Kunzelmann V, McDowell M T, Yu J, Larson D M, Borys N J, Abelyan C, Beeman J W and Yu K M 2016 *Nat. Commun.* **7** 12012
[70] Zhong M *et al* 2015 *J. Am. Chem. Soc.* **137** 5053
[71] Kuang Y *et al* 2016 *Nat. Energy* **2** 16191
[72] McDowell M T, Lichterman M F, Spurgeon J M, Hu S, Sharp I D, Brunschwig B S and Lewis N S 2014 *J. Phys. Chem.* C **118** 19618
[73] Sayama K, Nomura A, Zou Z, Abe R, Abe Y and Arakawa H 2003 *Chem. Commun.* **23** 2908
[74] Sayama K, Wang N, Miseki Y, Kusama H, Onozawa-Komatsuzaki N and Sugihara H 2010 *Chem. Lett.* **39** 17

[75] Luo W J, Yang Z S, Li Z S, Zhang J Y, Liu J G, Zhao Z Y, Wang Z Q, Yan S C, Yu T and Zou Z G 2011 *Energy Environ. Sci.* **4** 4046
[76] Kim T W, Ping Y, Galli G A and Choi K-S 2015 *Nat. Commun.* **6** 8769
[77] Qiu Y *et al* 2016 *Sci. Adv.* **2** e1501764
[78] Saito R, Miseki Y and Sayama K 2012 *Chem. Commun.* **48** 3833
[79] Su J, Guo L, Bao N and Grimes C A 2011 *Nano Lett.* **11** 1928
[80] Kosar S, Pihosh Y, Turkevych I, Mawatari K, Uemura J, Kazoe Y, Makita K, Sugaya T, Matsui T and Fujita D 2016 *Japan. J. Appl. Phys.* **55** 04ES01
[81] Kim J H, Jang J-W, Jo Y H, Abdi F F, Lee Y H, van de Krol R and Lee J S 2016 *Nat. Commun.* **7** 13380
[82] Shi X, Jeong H, Oh S J, Ma M, Zhang K, Kwon J, Choi I T, Choi I Y, Kim H K and Kim J K 2016 *Nat. Commun.* **7** 11943
[83] Kim J H, Jo Y, Kim J H, Jang J W, Kang H J, Lee Y H, Kim D S, Jun Y and Lee J S 2015 *ACS Nano* **9** 11820
[84] Chen Y-S, Manser J S and Kamat P V 2015 *J. Am. Chem. Soc.* **137** 974
[85] Kim J H, Kaneko H, Minegishi T, Kubota J, Domen K and Lee J S 2016 *ChemSusChem* **9** 61
[86] Shi X, Zhang K, Shin K, Ma M, Kwon J, Choi I T, Kim J K, Kim H K, Wang D H and Park J H 2015 *Nano Energy* **13** 182
[87] Seitz L C, Chen Z, Forman A J, Pinaud B A, Benck J D and Jaramillo T F 2014 *ChemSusChem* **7** 1372
[88] Prévot M S and Sivula K 2013 *J. Phys. Chem.* C **117** 17879
[89] Döscher H, Geisz J, Deutsch T and Turner J 2014 *Energy Environ. Sci.* **7** 2951
[90] Hu S, Xiang C, Haussener S, Berger A D and Lewis N S 2013 *Energy Environ. Sci.* **6** 2984
[91] Hu S, Shaner M R, Beardslee J A, Lichterman M, Brunschwig B S and Lewis N S 2014 *Science* **344** 1005
[92] Benck J D, Lee S C, Fong K D, Kibsgaard J, Sinclair R and Jaramillo T F 2014 *Adv. Energy Mater.* **4** 1400739
[93] McKone J R, Pieterick A P, Gray H B and Lewis N S 2013 *J. Am. Chem. Soc.* **135** 223
[94] Yu X, Prévot M S, Guijarro N and Sivula K 2015 *Nat. Commun.* **6** 7596
[95] Abe R, Higashi M and Domen K 2010 *J. Am. Chem. Soc.* **132** 11828
[96] Chun W-J, Isikawa A, Fujisawa H, Takata T, Kondo J N, Hara M, Kawai M, Matsumoto Y and Domen K 2003 *J. Phys. Chem.* B **107** 1798
[97] Hitoki G, Takata T, Kondo J N, Hara M, Kobayashi H and Domen K 1698 *Chem. Commun.* **16** 1698
[98] Higashi M, Domen K and Abe R 2012 *J. Am. Chem. Soc.* **134** 6968
[99] de Respinis M, Fravventura M, Abdi F F, Schreuders H, Savenije T J, Smith W A, Dam B and van de Krol R 2015 *Chem. Mater.* **27** 7091
[100] Lai K, Zhu Y, Lu J, Dai Y and Huang B 2013 *Solid State Sci.* **24** 79
[101] Vojvodic A, Medford A J, Studt F, Abild-Pedersen F, Khan T S, Bligaard T and Nørskov J K 2014 *Chem. Phys. Lett.* **598** 108
[102] Kandemir T, Schuster M E, Senyshyn A, Behrens M and Schlögl R 2013 *Angew. Chem. Int. Ed.* **52** 12723
[103] Wang G *et al* 2015 *Nano Lett.* **15** 4692
[104] Wang M, Ren F, Zhou J, Cai G, Cai L, Hu Y, Wang D, Liu Y, Guo L and Shen S 2015 *Sci. Rep.* **5** 12925
[105] Ghijsen J, Tjeng L H, van Elp J, Eskes H, Westerink J, Sawatzky G A and Czyzyk M T 1988 *Phys. Rev.* B **38** 11322
[106] Nakaoka K, Ueyama J and Ogura K 2004 *J. Electrochem. Soc.* **151** C661
[107] Meyer B K *et al* 2012 *Phys. Status Solidi* b **249** 1487
[108] Paracchino A, Brauer J C, Moser J-E, Thimsen E and Graetzel M 2012 *J. Phys. Chem.* C **116** 7341
[109] Brattain W H 1951 *Rev. Mod. Phys.* **23** 203
[110] Musa A O, Akomolafe T and Carter M J 1998 *Sol. Energy Mater. Sol. Cells* **51** 305
[111] Lee Y S, Winkler M T, Siah S C, Brandt R and Buonassisi T 2011 *Appl. Phys. Lett.* **98** 192115
[112] Hauffe K and Reinhold K 1972 *Ber. Bunsen-Ges. Phys. Chem.* **76** 616
[113] Gerischer H 1977 *J. Electroanal. Chem. Interfacial Electrochem.* **82** 133
[114] Chen S and Wang L-W 2012 *Chem. Mater.* **24** 3659
[115] Paracchino A, Laporte V, Sivula K, Grätzel M and Thimsen E 2011 *Nat. Mater.* **10** 456
[116] Morales-Guio C G, Liardet L, Mayer M T, Tilley S D, Grätzel M and Hu X 2015 *Angew. Chem. Int. Ed.* **54** 664
[117] Lin C-Y, Lai Y-H, Mersch D and Reisner E 2012 *Chem. Sci.* **3** 3482
[118] Zhang Z, Dua R, Zhang L, Zhu H, Zhang H and Wang P 2013 *ACS Nano* **7** 1709
[119] Li C, Hisatomi T, Watanabe O, Nakabayashi M, Shibata N, Domen K and Delaunay J-J 2015 *Energy Environ. Sci.* **8** 1493
[120] Luo J, Steier L, Son M-K, Schreier M, Mayer M T and Grätzel M 2016 *Nano Lett.* **16** 1848
[121] Sullivan I, Zoellner B and Maggard P A 2016 *Chem. Mater.* **28** 5999
[122] Sahoo P P, Zoellner B and Maggard P A 2015 *J. Mater. Chem.* A **3** 4501
[123] Kormányos A, Thomas A, Huda M N, Sarker P, Liu J P, Poudyal N, Janáky C and Rajeshwar K 2016 *J. Phys. Chem.* C **120** 16024
[124] Joshi U A and Maggard P A 2012 *J. Phys. Chem. Lett.* **3** 1577
[125] King N, Sahoo P P, Fuoco L, Stuart S, Dougherty D, Liu Y and Maggard P A 2014 *Chem. Mater.* **26** 2095
[126] Choi J, King N and Maggard P A 2013 *ACS Nano* **7** 1699
[127] Joshi U A, Palasyuk A M and Maggard P A 2011 *J. Phys. Chem.* C **115** 13534
[128] Zoellner B, Stuart S, Chung C-C, Dougherty D B, Jones J L and Maggard P A 2016 *J. Mater. Chem.* A **4** 3115
[129] King N, Sullivan I, Watkins-Curry P, Chan J Y and Maggard P A 2016 *J. Solid State Chem.* **236** 10
[130] Fuoco L, Joshi U A and Maggard P A 2012 *J. Phys. Chem.* C **116** 10490
[131] Kato H, Takeda A, Kobayashi M, Hara M and Kakihana M 2013 *Catal. Sci. Technol.* **3** 3147
[132] Sullivan I, Sahoo P P, Fuoco L, Hewitt A S, Stuart S, Dougherty D and Maggard P A 2014 *Chem. Mater.* **26** 6711
[133] Harb M, Masih D and Takanabe K 2014 *Phys. Chem. Chem. Phys.* **16** 18198
[134] Sheets W C, Mugnier E, Barnabé A, Marks T J and Poeppelmeier K R 2006 *Chem. Mater.* **18** 7
[135] Shin D *et al* 2009 *Phys. Rev.* B **80** 233105
[136] Kumar M, Zhao H and Persson C 2013 *Semicond. Sci. Technol.* **28** 065003
[137] Yanagi H, Hase T, Ibuki S, Ueda K and Hosono H 2001 *Appl. Phys. Lett.* **78** 1583
[138] Read C G, Park Y and Choi K-S 2012 *J. Phys. Chem. Lett.* **3** 1872
[139] Prévot M S, Guijarro N and Sivula K 2015 *ChemSusChem* **8** 1359
[140] Gu J, Wuttig A, Krizan J W, Hu Y, Detweiler Z M, Cava R J and Bocarsly A B 2013 *J. Phys. Chem.* C **117** 12415
[141] Prevot M S, Li Y, Guijarro N and Sivula K 2016 *J. Mater. Chem.* A **4** 3018
[142] Jang Y J, Park Y B, Kim H E, Choi Y H, Choi S H and Lee J S 2016 *Chem. Mater.* **28** 6054

[143] Benko F A and Koffyberg F P 1987 *J. Phys. Chem. Solids* **48** 431
[144] Snure M and Tiwari A 2007 *Appl. Phys. Lett.* **91** 092123
[145] Scanlon D O, Walsh A and Watson G W 2009 *Chem. Mater.* **21** 4568
[146] Scanlon D O and Watson G W 2011 *J. Mater. Chem.* **21** 3655
[147] Ueda K, Hase T, Yanagi H, Kawazoe H, Hosono H, Ohta H, Orita M and Hirano M 2001 *J. Appl. Phys.* **89** 1790
[148] Benko F A and Koffyberg F P 1986 *Phys. Status Solidi* a **94** 231
[149] Ginley D *et al* 2003 *Thin Solid Films* **445** 193
[150] Teplin C W, Kaydanova T, Young D L, Perkins J D, Ginley D S, Ode A and Readey D W 2004 *Appl. Phys. Lett.* **85** 3789
[151] Duan N, Sleight A W, Jayaraj M K and Tate J 2000 *Appl. Phys. Lett.* **77** 1325
[152] Nagarajan R, Duan N, Jayaraj M K, Li J, Vanaja K A, Yokochi A, Draeseke A, Tate J and Sleight A W 2001 *Int. J. Inorg. Mater.* **3** 265
[153] Koffyberg F P and Benko F A 1982 *J. Appl. Phys.* **53** 1173
[154] Li D, Hu J, Wu R and Lu J G 2010 *Nanotechnology* **21** 485502
[155] Nikam A V, Arulkashmir A, Krishnamoorthy K, Kulkarni A A and Prasad B L V 2014 *Cryst. Growth Des.* **14** 4329
[156] Sanal K C, Vikas L S and Jayaraj M K 2014 *Appl. Surf. Sci.* **297** 153
[157] Chauhan D, Satsangi V R, Dass S and Shrivastav R 2006 *Bull. Mater. Sci.* **29** 709
[158] Berglund S P, Lee H C, Nunez P D, Bard A J and Mullins C B 2013 *Phys. Chem. Chem. Phys.* **15** 4554
[159] Hardee K L and Bard A J 1977 *J. Electrochem. Soc.* **124** 215
[160] Jang Y J, Jang J-W, Choi S H, Kim J Y, Kim J H, Youn D H, Kim W Y, Han S and Sung Lee J 2015 *Nanoscale* **7** 7624
[161] Masudy-Panah S, Moakhar R S, Chua C S, Kushwaha A, Wong T I and Dalapati G K 2016 *RSC Adv.* **6** 29383
[162] Masudy-Panah S, Siavash Moakhar R, Chua C S, Tan H R, Wong T I, Chi D and Dalapati G K 2016 *ACS Appl. Mater. Interfaces* **8** 1206
[163] Lee J G, Kim D-Y, Lee J-H, Kim M-W, An S, Jo H S, Nervi C, Al-Deyab S S, Swihart M T and Yoon S S 2016 *ACS Appl. Mater. Interfaces* **8** 15406
[164] Kim M-W *et al* 2017 *Appl. Catal.* B **201** 479
[165] Septina W, Prabhakar R R, Wick R, Moehl T and Tilley S D 2017 *Chem. Mater.* **29** 1735
[166] Arai T, Konishi Y, Iwasaki Y, Sugihara H and Sayama K 2007 *J. Comb. Chem.* **9** 574
[167] Hahn N T, Holmberg V C, Korgel B A and Mullins C B 2012 *J. Phys. Chem.* C **116** 6459
[168] Berglund S P, Abdi F F, Bogdanoff P, Chemseddine A, Friedrich D and van de Krol R 2016 *Chem. Mater.* **28** 4231
[169] Ong E W, Kwei G H, Robinson R A, Ramakrishna B L and Von Dreele R B 1990 *Phys. Rev.* B **42** 4255
[170] Henmi C 1995 *Mineral. Mag.* **59** 545
[171] Klyndyuk A I, Petrov G S, Bashkirov L A, Akimov A I and Poluyan A F 1999 *Russ. J. Inorg. Chem.* **44** 1
[172] Kang D, Hill J C, Park Y and Choi K-S 2016 *Chem. Mater.* **28** 4331
[173] Cao D, Nasori N, Wang Z, Mi Y, Wen L, Yang Y, Qu S, Wang Z and Lei Y 2016 *J. Mater. Chem.* A **4** 8995
[174] Doumerc J P, Hejtmanek J, Chaminade J P, Pouchard M and Krussanova M 1984 *Phys. Status Solidi* a **82** 285
[175] Pyper K J, Yourey J E and Bartlett B M 2013 *J. Phys. Chem.* C **117** 24726
[176] Yourey J E, Pyper K J, Kurtz J B and Bartlett B M 2013 *J. Phys. Chem.* C **117** 8708
[177] Valenti M, Dolat D, Biskos G, Schmidt-Ott A and Smith W A 2015 *J. Phys. Chem.* C **119** 2096
[178] Gao Y, Zandi O and Hamann T W 2016 *J. Mater. Chem.* A **4** 2826
[179] Yourey J E and Bartlett B M 2011 *J. Mater. Chem.* **21** 7651
[180] Chang Y, Braun A, Deangelis A, Kaneshiro J and Gaillard N 2011 *J. Phys. Chem.* C **115** 25490
[181] Gaillard N, Chang Y, DeAngelis A, Higgins S and Braun A 2013 *Int. J. Hydrog. Energy* **38** 3166
[182] Bohra D and Smith W A 2015 *Phys. Chem. Chem. Phys.* **17** 9857
[183] Kihlborg L and Gebert E 1970 *Acta Crystallogr.* B **26** 1020
[184] Khyzhun O Y, Bekenev V and Solonin Y M 2009 *J. Alloys Compd.* **480** 184
[185] Khyzhun O Y, Strunskus T, Cramm S and Solonin Y M 2005 *J. Alloys Compd.* **389** 14
[186] Ruiz-Fuertes J, Errandonea D, Segura A, Manjón F, Zhu Z and Tu C 2008 *High Press. Res.* **28** 565
[187] Arora S, Mathew T and Batra N 1989 *J. Phys. Chem. Solids* **50** 665
[188] Bharati R, Singh R and Yadava Y 1983 *J. Mater. Sci. Lett.* **2** 623
[189] Bharati R, Shanker R and Singh R 1980 *Pramana* **14** 449
[190] Khader M M, Saleh M M and El-Naggar E M 1998 *J. Solid State Electrochem.* **2** 170
[191] Leiva H, Dwight K and Wold A 1982 *J. Solid State Chem.* **42** 41
[192] Bharati R and Singh R 1981 *J. Mater. Sci.* **16** 511
[193] Abdi F F, Chemseddine A, Berglund S P and van de Krol R 2017 *J. Phys. Chem.* C **121** 153
[194] Abdi F F, Berglund S P and van de Krol R 2016 *Photoelectrochemical Solar Fuel Production* (Berlin: Springer) p 355
[195] Harb M, Ziani A and Takanabe K 2016 *Phys. Status Solidi* b **253** 1115
[196] Kuzmin A, Anspoks A, Kalinko A, Timoshenko J and Kalendarev R 2015 *Sol. Energy Mater. Sol. Cells* **143** 627
[197] Jeitschko W and Sleight A W 1972 *Acta Crystallogr.* B **28** 3174
[198] Ziani A, Harb M, Noureldine D and Takanabe K 2015 *APL Mater.* **3** 096101
[199] Cho I-S, Kwak C H, Kim D W, Lee S and Hong K S 2009 *J. Phys. Chem.* C **113** 10647
[200] Noureldine D, Anjum D H and Takanabe K 2014 *Phys. Chem. Chem. Phys.* **16** 10762
[201] Hosogi Y, Shimodaira Y, Kato H, Kobayashi H and Kudo A 2008 *Chem. Mater.* **20** 1299
[202] Liu Y, Ma J, Dai C, Song Z, Sun Y, Fang J, Gao C and Zhao J 2009 *J. Am. Ceram. Soc.* **92** 2791
[203] Mohamed R M, Harraz F A and Mkhalid I A 2012 *J. Alloys Compd.* **532** 55
[204] Enache C S, Lloyd D, Damen M R, Schoonman J and van de Krol R 2009 *J. Phys. Chem.* C **113** 19351
[205] van de Krol R, Ségalini J and Enache C S 2011 *J. Photon. Energy* **1** 016001
[206] Morton C D, Slipper I J, Thomas M J and Alexander B D 2010 *J. Photochem. Photobiol.* A **216** 209
[207] Biswas S K and Baeg J-O 2013 *Int. J. Hydrog. Energy* **38** 14451
[208] Jain A *et al* 2013 *APL Mater.* **1** 011002
[209] Gupta S, Yadava Y P and Singh R A 1986 *J. Mater. Sci. Lett.* **5** 736
[210] Mandal H, Shyamal S, Hajra P, Bera A, Sariket D, Kundu S and Bhattacharya C 2016 *RSC Adv.* **6** 4992
[211] Tang D, Rettie A J E, Mabayoje O, Wygant B R, Lai Y, Liu Y and Mullins C B 2016 *J. Mater. Chem.* A **4** 3034
[212] Yan Q, Li G, Newhouse P F, Yu J, Persson K A, Gregoire J M and Neaton J B 2015 *Adv. Energy Mater.* **5** 1401840
[213] Zhou L *et al* 2015 *Adv. Energy Mater.* **5** 1500968
[214] He Z and Ueda Y 2008 *J. Solid State Chem.* **181** 235
[215] Liao J H, Leroux F, Piffard Y, Guyomard D and Payen C 1996 *J. Solid State Chem.* **121** 214

[216] Medvedeva N I, Rotermel M V and Krasnenko T I 2015 *Phys. Status Solidi* b **252** 2853
[217] Fleury P 1966 *C. R. Hebd. Seances Acad. Sci.* C **263** 1375
[218] Brisi C M 1958 *Ann. Chim. Roma* **48** 263
[219] Birnie D P, Weinberg J D and Swanson D G 1992 *J. Mater. Res.* **7** 741
[220] Kawada T, Hinokuma S and Machida M 2015 *Catal. Today* **242** 268
[221] Kawada T, Tajiri T, Yamashita H and Machida M 2014 *Catal. Sci. Technol.* **4** 780
[222] Machida M, Miyazaki Y, Matsunaga Y and Ikeue K 2011 *Chem. Commun.* **47** 9591
[223] Zhang S Y, Sun Y, Li C S and Ci L J 2013 *Solid State Sci.* **25** 15
[224] Hillel T and Ein-Eli Y 2013 *J. Power Sources* **229** 112
[225] Guo W, Chemelewski W D, Mabayoje O, Xiao P, Zhang Y and Mullins C B 2015 *J. Phys. Chem.* C **119** 27220
[226] Seabold J A and Neale N R 2015 *Chem. Mater.* **27** 1005
[227] Newhouse P F, Boyd D A, Shinde A, Guevarra D, Zhou L, Soedarmadji E, Li G, Neaton J B and Gregoire J M 2016 *J. Mater. Chem.* A **4** 7483
[228] Zhou L *et al* 2016 *Phys. Chem. Chem. Phys.* **18** 9349
[229] Wang M and Liu Q 2011 *Adv. Mater. Res.* **236–238** 1675–8
[230] Sickafus K E, Wills J M and Grimes N W 1975 *J. Am. Ceram. Soc.* **82** 3279
[231] Grimes N W 1975 *Phys. Technol.* **6** 22
[232] Boumaza S, Bouarab R, Trari M and Bouguelia A 2009 *Energy Convers. Manage.* **50** 62
[233] Salavati-Niasari M, Davar F and Farhadi M 2009 *J. Sol-Gel Sci. Technol.* **51** 48
[234] Köferstein R, Walther T, Hesse D and Ebbinghaus S G 2014 *J. Solid State Chem.* **213** 57
[235] Boudjemaa A, Bouarab R, Saadi S, Bouguelia A and Trari M 2009 *Appl. Energy* **86** 1080
[236] Rekhila G, Bessekhouad Y and Trari M 2013 *Int. J. Hydro. Energy* **38** 6335
[237] Chervin C N, DeSario P A, Parker J F, Nelson E S, Miller B W, Rolison D R and Long J W 2016 *ChemElectroChem* **3** 1369
[238] Bao J, Zhang X, Fan B, Zhang J, Zhou M, Yang W, Hu X, Wang H, Pan B and Xie Y 2015 *Angew. Chem. Int. Ed.* **54** 7399
[239] Peng Z, Jia D, Al-Enizi A M, Elzatahry A A and Zheng G 2015 *Adv. Energy Mater.* **5** 1402031
[240] Xu Z, Yan S-C, Shi Z, Yao Y-F, Zhou P, Wang H-Y and Zou Z-G 2016 *ACS Appl. Mater. Interfaces* **8** 12887
[241] Matsumoto Y, Omae M, Sugiyama K and Sato E 1987 *J. Phys. Chem.* **91** 577
[242] Ida S, Yamada K, Matsunaga T, Hagiwara H, Matsumoto Y and Ishihara T 2010 *J. Am. Chem. Soc.* **132** 17343
[243] Matsumoto Y, Sugiyama K and Sato E-I 1988 *J. Solid State Chem.* **74** 117
[244] Díez-García M I and Gómez R 2016 *ACS Appl. Mater. Interfaces* **8** 21387
[245] Sekizawa K, Nonaka T, Arai T and Morikawa T 2014 *ACS Appl. Mater. Interfaces* **6** 10969
[246] Ahmed M G, Kandiel T A, Ahmed A Y, Kretschmer I, Rashwan F and Bahnemann D 2015 *J. Phys. Chem.* C **119** 5864
[247] Kim E S, Nishimura N, Magesh G, Kim J Y, Jang J-W, Jun H, Kubota J, Domen K and Lee J S 2013 *J. Am. Chem. Soc.* 5375
[248] Kim J H, Kim J H, Jang J-W, Kim J Y, Choi S H, Magesh G, Lee J and Lee J S 2015 *Adv. Energy Mater.* **5** 1401933
[249] Matsumoto Y 1996 *J.Solid State Chem.* **126** 227
[250] McDonald K J and Choi K-S 2011 *Chem. Mater.* **23** 4863
[251] Yao J, Li X, Li Y and Le S 2013 *Integr. Ferroelectr.* **145** 17
[252] De Haart L G J and Blasse G 1985 *Solid State Ion.* **16** 137
[253] Hufnagel A G, Peters K, Müller A, Scheu C, Fattakhova-Rohlfing D and Bein T 2016 *Adv. Funct. Mater.* **26** 4435
[254] Takaobushi J *et al* 2006 *Appl. Phys. Lett.* **89** 242507
[255] Lorenz M, Brandt M, Mexner K, Brachwitz K, Ziese M, Esquinazi P, Hochmuth H and Grundmann M 2011 *Phys. Status Solidi* **5** 438
[256] Bosman A J and Vandaal H J 1970 *Adv. Phys.* **19** 1
[257] Kim J H, Jang Y J, Kim J H, Jang J-W, Choi S H and Lee J S 2015 *Nanoscale* **7** 19144
[258] Lettmann C, Hinrichs H and Maier W F 2001 *Angew. Chem. Int. Ed.* **40** 3160
[259] Skorupska K and Parkinson B A 2016 *Photoelectrochemical Solar Fuel Production: From Basic Principles to Advanced Devices* ed S Giménez and J Bisquert (Berlin: Springer) p 427
[260] Woodhouse M and Parkinson B A 2008 *Chem. Mater.* **20** 2495
[261] Walsh A, Wei S-H, Yan Y, Al-Jassim M M, Turner J A, Woodhouse M and Parkinson B A 2007 *Phys. Rev.* B **76** 165119
[262] Newhouse P F and Parkinson B A 2015 *J. Mater. Chem.* A **3** 5901
[263] Sliozberg K, Stein H S, Khare C, Parkinson B A, Ludwig A and Schuhmann W 2015 *ACS Appl. Mater. Interfaces* **7** 4883
[264] Kondofersky I, Müller A, Dunn H K, Ivanova A, Štefanic G, Ehrensperger M, Scheu C, Parkinson B A, Fattakhova-Rohlfing D and Bein T 2016 *J. Am. Chem. Soc.* **138** 1860
[265] Haber J A, Cai Y, Jung S, Xiang C, Mitrovic S, Jin J, Bell A T and Gregoire J M 2014 *Energy Environ. Sci.* **7** 682
[266] Guevarra D, Shinde A, Suram S K, Sharp I D, Toma F M, Haber J A and Gregoire J M 2016 *Energy Environ. Sci.* **9** 565
[267] Shinde A, Guevarra D, Liu G, Sharp I D, Toma F M, Gregoire J M and Haber J A 2016 *ACS Appl. Mater. Interfaces* **8** 23696
[268] Shinde A, Jones R J R, Guevarra D, Mitrovic S, Becerra-Stasiewicz N, Haber J A, Jin J and Gregoire J M 2015 *Electrocatalysis* **6** 229
[269] Xiang C, Haber J, Marcin M, Mitrovic S, Jin J and Gregoire J M 2014 *ACS Comb. Sci.* **16** 120
[270] Suram S K, Newhouse P F and Gregoire J M 2016 *ACS Comb. Sci.* **18** 673
[271] Suram S K, Newhouse P F, Zhou L, Van Campen D G, Mehta A and Gregoire J M 2016 *ACS Comb. Sci.* **18** 682
[272] Greeley J, Jaramillo T F, Bonde J, Chorkendorff I and Nørskov J K 2006 *Nat. Mater.* **5** 909
[273] Curtarolo S, Hart G L W, Nardelli M B, Mingo N, Sanvito S and Levy O 2013 *Nat. Mater.* **12** 191
[274] Gardner R F G, Sweett F and Tanner D W 1963 *J. Phys. Chem. Solids* **24** 1183
[275] Guo X, Wang L and Tan Y 2015 *Nano Energy* **16** 320
[276] Tahir A A and Wijayantha K G U 2010 *J. Photochem. Photobiol.* A **216** 119
[277] Hodby J W, Jenkins T E, Schwab C, Tamura H and Trivich D 1976 *J. Phys. C: Solid State Phys.* **9** 1429
[278] Malerba C, Biccari F, Leonor Azanza Ricardo C, D'Incau M, Scardi P and Mittiga A 2011 *So. Energy Mater. Sol. Cells* **95** 2848